energies

MDPI

Article

Multiple Input-Single Output DC-DC Converters Assessment for Low Power Renewable Sources Integration

Joaquin Soldado-Guamán [1], Victor Herrera-Perez [2,*], Mayra Pacheco-Cunduri [3], Alejandro Paredes-Camacho [4], Miguel Delgado-Prieto [4] and Jorge Hernandez-Ambato [3]

[1] Independent Researcher, Riobamba 060101, Ecuador
[2] Colegio de Ciencias e Ingenierías, Universidad San Francisco de Quito—USFQ, Quito 170901, Ecuador
[3] Facultad de Informática y Electrónica, Escuela Superior Politécnica de Chimborazo (ESPOCH), Riobamba 060101, Ecuador
[4] Departamento de Ingeniería Electrónica, Grupo de Investigación MCIA, Universitat Politécnica de Catalunya—UPC, 08222 Barcelona, Spain
* Correspondence: vherrera@usfq.edu.ec

Abstract: This paper presents a comparison of Isolated (Flyback) and non-Isolated (Buck) multiple input-single output (MISO) DC-DC converters. The analysis of DC-DC converters is based on pulsed voltage source cells (PVSC). The modeling of both converter types is detailed through their mathematical models and electrical simulations using Matlab/Simulink and PSIM. The comparison focuses on the sizing parameters, non-ideal output characteristics and efficiency. Results show that the output voltage of the MISO Buck converter exhibits a linear dependence on the duty cycles control signal and has slightly higher efficiency than the Flyback converter. To validate the operation of both converters, a scenario with two inputs (low-power hydroelectric and photovoltaic voltage sources) is considered. The modeling and control of both source systems are detailed and the MISO converter performance response is evaluated under sources changes and efficiency point of view.

Keywords: DC-DC converter; isolated converter; MISO converter; multiport converter; low power renewable sources

check for updates

Citation: Soldado-Guamán, J.; Herrera-Perez, V.; Pacheco-Cunduri, M.; Paredes-Camacho, A.; Delgado-Prieto, M.; Hernandez-Ambato, J. Multiple Input-Single Output DC-DC Converters Assessment for Low Power Renewable Sources Integration. *Energies* **2023**, *16*, 1652. https://doi.org/10.3390/en16041652

Academic Editors: Ignacio Hernando-Gil, Ionel Vechiu and Elyas Rakhshani

Received: 31 December 2022
Revised: 26 January 2023
Accepted: 3 February 2023
Published: 7 February 2023

Copyright: © 2023 by the authors. Licensee MDPI, Basel, Switzerland. This article is an open access article distributed under the terms and conditions of the Creative Commons Attribution (CC BY) license (https://creativecommons.org/licenses/by/4.0/).

1. Introduction

The development of societies worldwide is directly linked to their energy consumption, which is why growing societies represent an increasing demand for energy [1]. The current environmental concerns and the non-sustainability in the use of non-renewable resources make energy generation through the consumption of fossil fuels less and less feasible, and this is how the eradication of dangerous methods for energy generation is becoming a contemporary requirement around the world [2].

The renewable energy sources available in nature, such as solar, hydroelectric, wind, etc. that are not polluting are considered alternatives to fossil fuels. Thus, they have become the most emerging method of power generation worldwide to meet the current power demand [3]. However, despite the countless advantages that their use represents, there are certain factors to consider, for example that these sources are not continuously available, and they are unstable and discontinuous due to weather conditions; for this reason, in order to counteract these drawbacks and make better use of them, hybrid systems are a suitable option, for which the use of power electronics interfaces has become essential, thus developing numerous converter topologies together with control techniques to make them more robust and efficient [4,5].

Hybrid renewable energy systems are generally implemented by integrating multiple sources of renewable energy generation to build a high-quality energy generation system that is independent, efficient, and robust [6]. These systems are composed of various input power sources, integrated through multi-input power electronics converters that

could accommodate a variety of input sources and combine their advantages to offer controlled output for diversified applications (multiple input, single output (MISO) DC-DC converters) [7]. Converters are the most significant part of any hybrid renewable energy system due to their ability to stabilize the voltage output during intermittent conditions [8].

Multiple input, single output (MISO) DC-DC converters are classified into two categories (a) isolated and (b) non-isolated converters. Isolated converters [9] isolate the low-voltage DC side from the high-voltage side to avoid the risk of electric shock, achieve high-voltage conversion, equalize the voltage, and bypass large current/voltage rating semiconductor devices, using, for this purpose, high-frequency transformers. However, the downside to this system is that it needs to accommodate a transformer core, which makes it bulky and, in terms, adds to the cost. On the other hand, non-isolated converters are simple in structure and are used where galvanic isolation between load and source is not required. Non-isolated converters can match the input impedance of the source and the output impedance of the load, but these converters cannot achieve a high-voltage conversion ratio [10]. In renewable energy systems, the power quality depends to a large extent on the stable operation of the power converter [11]; however, most conventional converters and control techniques, as mentioned, have several drawbacks that overshadow their effectiveness. Thus, the design of improved multiple input, single output (MISO) DC-DC converters and more effective control techniques is a pressing need in renewable energy generation.

According to the literature, there are various designs for this type of power converter, and their relevant characteristics are analyzed below. The basic designs of the DC-DC step-up converters are conventional boost converters, for which the design includes one inductor, one power switch, and one power diode; since the structure of this converter is simple, and the interleaved structures have not been considered for these topologies, they are mainly used for low-power applications [12]. Fly-back converter's efficiency is not considerable compared with the new high-gain and high-efficiency designs due to the use of the transformer in their design that leads to the heavy and large structures. Other designs of converters in the same way that Fly-back uses the transformer, the input DC voltage normally by a resonant circuit or an inverter is converted to the AC voltage. An AC voltage with a higher magnitude is obtained for the next step at the secondary side of the transformer. Then, this voltage is converted to the DC voltage with the desired amplitude by a rectifier block. Therefore, these types of converters' efficiency is impressed by the high number of the middle blocks and components in the converter [13]. Push–pull converts are selected when galvanic isolation is required or when the ratio between input and output voltage is high enough to bring in some safety concerns. Isolated converters such as Fly-back and Push–Pull are based on the existing transformer in their structure; the ground of the sections before and after the transformer is different and separate. Therefore, it needs more components and approaches for load connections. The principal problem of these converters lies in leakage inductor, and according to solve it, an active-clamp and snubber topologies should be added to the converter, which increases the number of components and cost of the circuit and decreases the efficiency of these topologies [14]. A Buck–Boost single inductor converter provides an output voltage that can be either higher or lower than the input voltage; in addition, a negative-polarity output is obtained concerning the common terminal of the input current. The main advantage of Buck–Boost single inductor converter is the low number of devices used to achieve the conversion [15].

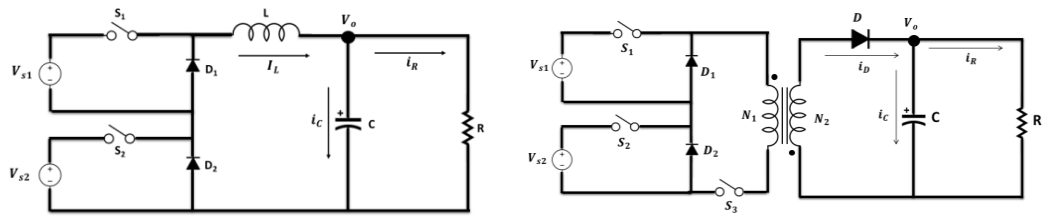
The use of multiple input, single output (MISO) DC-DC converters has been analyzed in multiple works [16], which propose a switched capacitor (SC)-based quadratic boost converter (QBC) structure that provides high-voltage gain at low duty cycles equipped with the fuzzy logic control (FLC) technique. In [17], an analysis and controller design of a double-input DC-DC converter (DIDDC) is introduced. Ref. [18] shows a new topology of multiple-input single-output PV system for DC load applications. A review of multiple input DC-DC converter topologies linked with hybrid electric vehicles and renewable energy systems is developed in [19]. The study of a highly efficient DC-DC boost converter

implemented with an improved MPPT algorithm for utility level photovoltaic applications is proposed in [20], and a step-up multiple-input multi-stage DC-DC converter with a soft-switching for Photovoltaic (PV) applications is presented in [21]. The contemporary development, recent advances, and characteristics of multiple input DC-DC converters are identified, examined, and analyzed in [22]. On the one hand, MISO solutions focus on connecting multiple inputs through a high-frequency transformer, which represents an intermediate DC-DC conversion, as reported in [21,22]. The main advantage of such a topology converter is related to electrical isolation and magnetic coupling between all converter ports. However, it requires a specific design and a high-frequency multi-winding transformer. On the other hand, the integration of different DC voltage sources on a common bus through single input, single output (SISO) DC-DC converters is also an option to implement MISO converters, as reported in [23,24]. However, the former result in complex systems with multiple components and a complex control structure. Another approach for multiple input DC-DC converter solutions is to couple multiple pulsed source cells as reported. The sources can be current or pulsed voltage cells, designed after primary DC-DC converters. This alternative reduces the number of components, presents compact structures, and allows simultaneous or independent operation of the power supplies [7].

This document presents an analysis and comparative evaluation of multiple input, single output (MISO) DC-DC converters based on pulsed voltage source cells (PVSC) for the integration of different low-power sources of renewable energy. To this end, the case studies are proposed grouping them according to the type of connection between sources and loads, which can be electrical or magnetic, isolated (Flyback), and non-isolated (Buck) converters. It begins by presenting the synthesis of multiport DC-DC converters through the integration of PVSC, emphasizing the modeling and dimensioning of each case study based on the ideal and non-ideal analysis of current and voltage inductor and capacitor of filtering output circuits, and the output voltage of converters as well. Simulation tools such as Matlab/Simulink and PSIM are used. In addition, to validate the operation of both converters, a scenario with two inputs is considered (low-power hydroelectric and photovoltaic voltage sources), and the incidence of non-ideal elements in said converters is analyzed, focusing the comparison on sizing parameters, characteristics output, and efficiency of the converters. Finally, the efficiency results of multiport DC-DC converters designed for a case study are presented, evaluating the performance response of the MISO converters under load and sources changes.

2. Methodology

Taking into account the information presented so far as state of the art, this paper aims to analyze the design and operation of four different MISO converters based on design strategy by pulsating voltage source cells (PVSC). On the one hand, the topology of a Buck-type DC-DC MISO converter is presented in Figure 1a [25]. On the other hand, the topology of a MISO Flyback DC-DC converter is shown in Figure 1b [26]. The main difference between these two MISO converters is the presence of a high-frequency transformer, which offers electric isolation for input voltage sources and load.



(**a**) MISO Buck converter (**b**) MISO Flyback converter

Figure 1. Non-isolated and isolated DC-DC MISO converters topologies.

The next subsections deal with the particular study of each of the aforementioned converters, prioritizing the analysis for establishing the sizing and efficiency parameters of

each DC-DC MISO converter. Finally, design and analysis of a case study for integration of low-power renewable sources evaluation, through such MISO converters, is described.

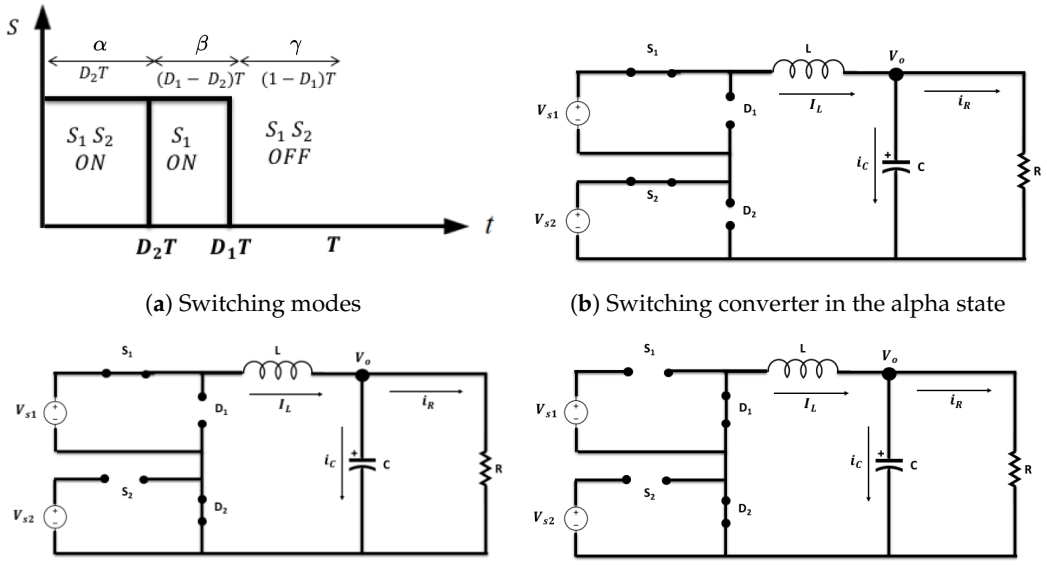
2.1. Modelling of MISO DC-DC Converters

As a first part, models of MISO DC-DC converters are defined through equations that characterize their electric behavior. The analysis criteria of ideal conditions has been considered for the continues current mode (CCM). Therefore, the following conditions have been considered: (1) The current in the inductor is permanent and greater than zero. (2) The average voltage in the inductor is null in each period. (3) The average current in the output capacitor is zero. (4) The power delivered by the source is equal to that supplied to the load. (5) The topology of the case study operates in steady state and at full load. (6) The value of the capacitor is very large capable of keeping the output voltage constant.

Furthermore, it is worth mentioning that, to facilitate the analysis, duty cycle for switch S2 (D_2) is higher than for switch S1 (D_1); therefore, voltage source 1 (V_{S1}) delivers power to the load during more time than voltage source 2 (V_{S2}).

2.1.1. MISO Buck Converter

Definition of the switching strategy, for the converter presented in Figure 1a, is proposed in Figure 2a. The switching period starts with switches S1 and S2 turned-on until D_2T, which represents α state, while diodes D1 and D2 are blocking current (see Figure 2b). Then, switch S2 is turned-off, while diode D2 is conducting current, until D_1T time representing β state (see Figure 2c). For the remaining period time, switch S1 is also turned-off, while diode D1 conducts a current, which is represented by the γ state (see Figure 2d). Relation between the switching modes, schematic circuits, and inductor voltage and current variation equations are summarized in Table 1.



(**a**) Switching modes

(**b**) Switching converter in the alpha state

(**c**) Switching converter in the beta state

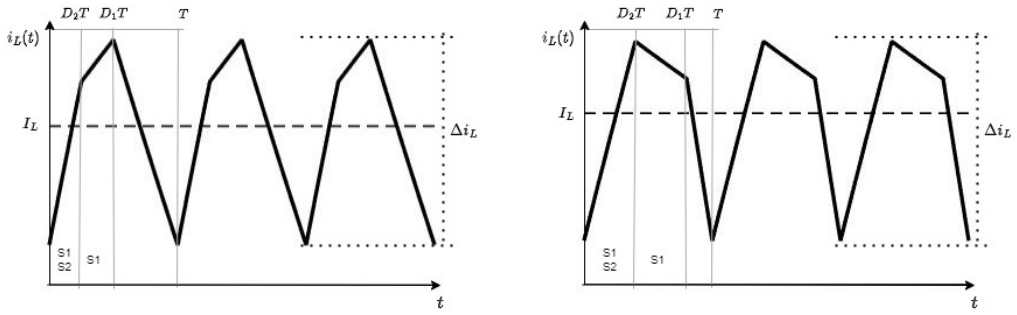
(**d**) Switching converter in the gamma state

Figure 2. Switching strategy and states of the MISO Buck DC-DC converter.

Table 1. Voltage and current inductor equations for MISO Buck converter.

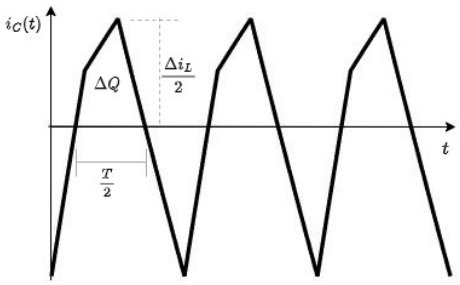
States	S1	S2	Inductor Voltage (V_L)	Inductor Current Change (Δi_L)
Alpha (α)	On	On	$V_L = V_{S1} + V_{S2} - V_o$	$\Delta i_L = (V_{S1} + V_{S2} - V_o)/L)D_2T$
Beta (β)	On	Off	$V_L = V_{S1} - V_o$	$\Delta i_L = (V_{S1} - V_o)/L)(D_1D_2)T$
Gamma (γ)	Off	Off	$V_L = -V_o$	$\Delta i_L = (-V_o)/L)(1D_1)T$

According to the switching modes for MISO buck converter, the inductor current (i_L) curve is shown in Figure 3a, according to the condition $V_o < V_{S1}$, while for the condition $V_o \geq V_{S1}$, then the inductor current curve is shown in Figure 3b. In both cases, i_L increases rapidly from minimum value during α state, while the current decreases again to a minimum during γ state. However, during β state, i_L can keep increasing until it reaches the maximum or starts decreasing from maximum, depending on the output voltage value.

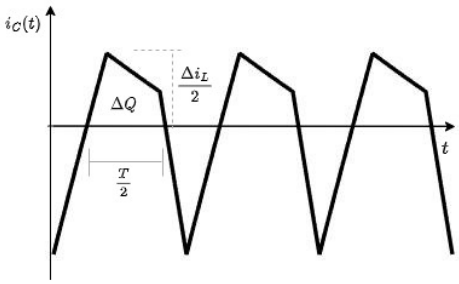


(**a**) Inductor's current for $V_o \leq V_{s1}$

(**b**) Inductor's current for $V_o \geq V_{s1}$



(**c**) Capacitor's current for $V_o \leq V_{s1}$



(**d**) Capacitor's current for $V_o \geq V_{s1}$

Figure 3. Characteristic current curves of the MISO Buck converter for different output voltage conditions.

Considering the data shown in Table 1 and Figure 3, with $(\Delta i_L)_\alpha + (\Delta i_L)_\beta + (\Delta i_L)_\gamma = 0$, the output voltage is defined by (1), while the mean inductor current is the same as for load resistance current (I_R), which is calculated using (2).

$$V_o = D_1 \cdot V_{S1} + D_2 \cdot V_{S2} \tag{1}$$

$$I_L = I_R = \frac{V_o}{R} \tag{2}$$

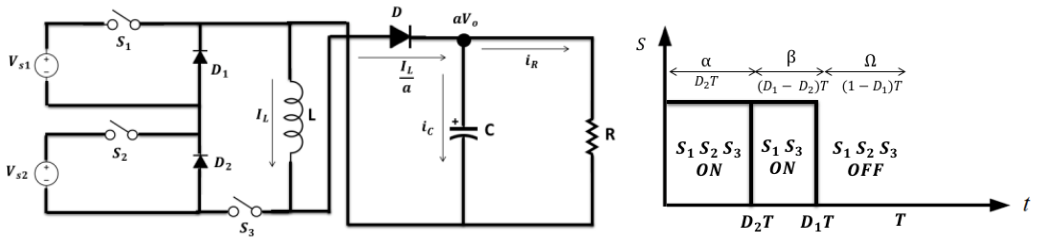
Finally, designing equations for filtering inductor and output capacitor values are defined by (3) and (4), respectively. Such equations depend on the desired inductor current ripple (Δi_{L_m}) and output voltage ripple (ΔV_o), where F_{sw} is the switching frequency of the control signal:

$$L_{min} = Max\left[\frac{V_o(1D_1)}{\Delta i_L F_{sw}}, \frac{(V_{S1} + V_{S2} - V_o)D_2}{\Delta i_L F_{sw}}\right] \tag{3}$$

$$C_{min} = Max\left[\frac{V_o(1D_1)}{8LF_{sw}^2 \Delta V_o}, \frac{(V_{S1} + V_{S2} - V_o)D_2}{8LF_{sw}^2 \Delta V_o}\right] \tag{4}$$

2.1.2. MISO Flyback Converter

The schematic of this converter was presented in Figure 1b; however, analysis is carried out on the equivalent circuit of the MISO Flyback converter shown in Figure 4a. The switching strategy for MISO Flyback DC-DC converter is illustrated in Figure 4b.

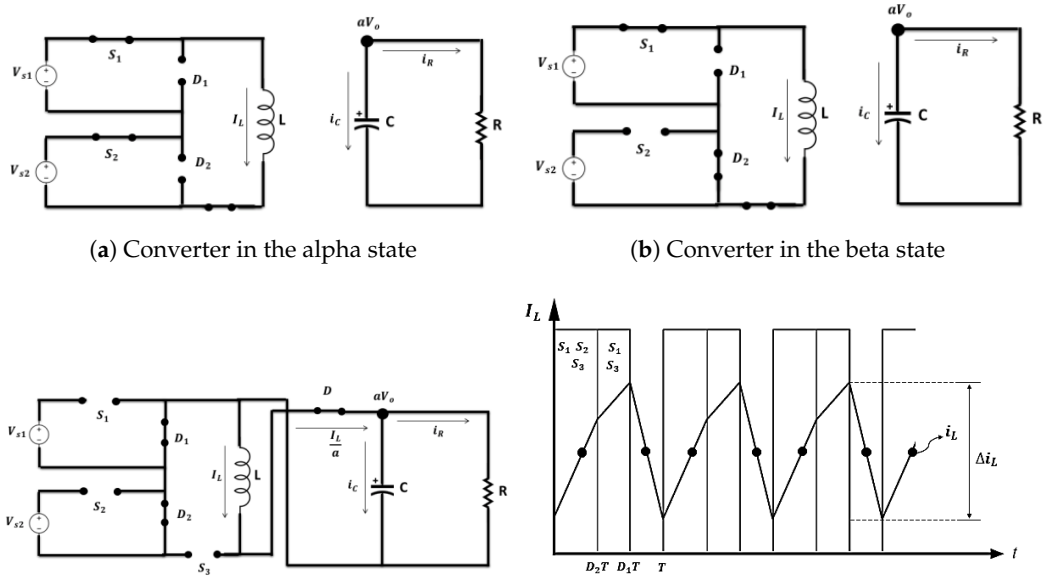


(**a**) Equivalent circuit of the Flyback converter (**b**) Switching modes

Figure 4. Switching strategy for analysis of MISO Flyback DC-DC converters.

During α state, S1, S2 and S3 switches are turned-on with diodes D1 and D2 disconnected during D_2T, as presented in Figure 5a. Then, in β state, only S2 is turned-off while diode D2 is conducting current until D_1T, as shown in Figure 5b. The last of the period is denoted as Ω state, and all the switches are turned-off allowing for current induction flowing to the output circuit as shown in Figure 5c.

Different from the last two analyzed converters, the magnetizing inductor current has only one waveform type, independent of output voltage level, which is described in Figure 5d.



(**a**) Converter in the alpha state (**b**) Converter in the beta state

(**c**) Converter in the omega state (**d**) Magnetizing inductor's current waveform

Figure 5. Circuit states and inductor current waveform of the MISO Flyback DC-DC converter.

In Table 2, a summary of switches states, magnetizing voltage and current changes equations for each switching state is presented.

Table 2. Voltage and current inductor equations for the MISO Flyback converter.

States	S1	S2	S3	Inductor Votlage (V_L)	Inductor Current Change (ΔI_L)
Alpha	On	On	On	$V_L = V_{S1} + V_{S2}$	$\Delta I_L = ((V_{s1} + V_{s2})/L)D_2T$
Beta	On	Off	On	$V_L = V_{S1}$	$\Delta I_L = (V_{s1}/L)(D_1D_2)T$
Omega	Off	Off	Off	$V_L = -aV_o$	$\Delta I_L = (-aV_o/L)(1D_1)T$

Using the same criteria of inductor change current equilibrium ($\Delta i_{L_\alpha} + \Delta i_{L_\beta} + \Delta i_{L_\Omega} = 0$) and information from Figure 5 and Table 2, the output voltage V_o for MISO Flyback DC-DC

converter is defined by (5), while the mean magnetizing inductor current I_L is calculated through (6), where a is the transformer turns ratio (N_1/N_2), and R is the load resistance:

$$V_o = \frac{D_1 V_{S1} + D_2 V_{S2}}{a(1D_1)} \tag{5}$$

$$I_L = \frac{D_1 V_{S1} + D_2 V_{S2}}{Ra^2(1D_1)^2} \tag{6}$$

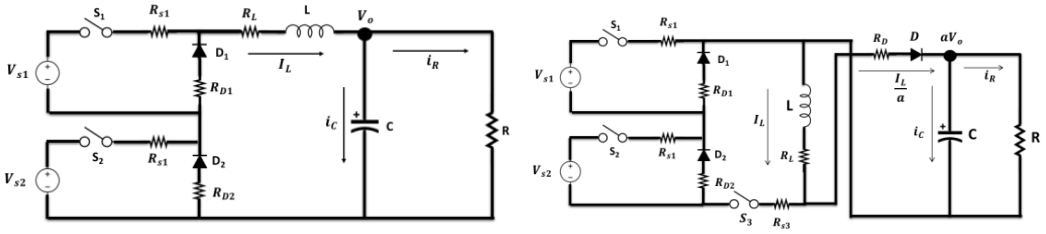
Finally, designing equations for magnetizing inductor and output capacitor values are defined by (7) and (8), respectively, depending on the desired inductor current ripple (Δi_L) and desired output voltage ripple (ΔV_o), where, F_{sw} is the switching frequency of the control signal

$$L_{min} = \frac{V_{S1} D_1 + V_{S2} D_2}{\Delta i_L F_{sw}} \tag{7}$$

$$C_{min} = \frac{D_1 V_o}{R F_{sw} \Delta V_o} \tag{8}$$

2.2. Non-Idealities on MISO DC-DC Converters

The devices that are part of the topology of any type of power electronics system usually present a behavior that is far from the ideal operation. These non-ideal behaviors of electronic devices lead to power losses which significantly affect the power transfer, as well as differences on the output voltage. To estimate the effect of losses on MISO Buck and Flyback DC-DC converters, the study use a modelling approach focused on the equivalent circuit converters presented in Figure 6, which incorporate all possible undesired parasitic resistances.



(**a**) Non-ideal MISO Buck converter (**b**) Non-ideal MISO Flyback converter

Figure 6. Cases study considered for the analysis of non-ideal effects.

2.2.1. Nonlinear Output Voltage

Within this study, the voltage drops associated with the resistivity of the main electronic components are considered. However, there are other factors that can generate voltage drops due to the operating environment. These types of losses are not usually considered due to the difficulty of quantifying their value within a given operating regime and/or because they are of insignificant magnitude.

Figure 6 shows a non-ideal equivalent circuit of the analyzed MISO converters, where R_{S1},R_{S2},R_{D1},R_{D2} and R_L are the resistances of the switches, diodes and inductor, respectively. These resistive elements represent the conduction losses of the system. Through similar analysis performed in Sections 2.1.1 and 2.1.2, Equations (9) and (10) are obtained, which approximate the real behavior of the MISO Buck and Flyback DC-DC converters, respectively:

$$V_{o_{Buck}} = \frac{D_1 V_{S1} + D_2 V_{S2}}{1 + \frac{R_L + R_{D2}(1D_2) + R_{D1}(1D_1) + R_{S1}D_1 + R_{S2}D_2}{R}} \tag{9}$$

$$V_{o_{Flyback}} = \frac{D_1 V_{S1} + D_2 V_{S2}}{a\left(1D_1 + \frac{R_{D2}(D_1 - D_2) + D_2 R_{S2} + D_1 R_{S1} + R_L D_1 + R_{S3} D_1 + \frac{(1D_1)(R_L + R_{D3})}{a}}{R(1D_1)a}\right)} \tag{10}$$

2.2.2. Dynamical Modelling of MISO DC-DC Buck Converters

In order to obtain the set of equations to describe the dynamic behaviour of the MISO Buck and Flyback DC-DC converters, an analysis using the superposition principle is performed considering the different switching states of the converters (see Figures 2 and 4). In every switching state, the analysis is oriented to find two dynamic equations: current on inductor and voltage on output capacitor.

On the one hand, the inductor current and output voltage for MISO DC-DC Buck converter represented in Figure 6a, for α, β and γ states, are presented in Equations (11)–(13), respectively. Then, such equations are combined through the addition and proportionality properties of the system to simplify the equations system to more simple expressions as shown in Equation (14):

$$\begin{cases} L\frac{di_{L_\alpha}}{dt} &= V_{S1} + V_{S2} - (R_{S1} + R_{S2} + R_L)I_L(t) - V_o(t) \\ C\frac{dV_{o_\alpha}}{dt} &= I_L(t) - \frac{V_o(t)}{R} \end{cases} \tag{11}$$

$$\begin{cases} L\frac{di_{L_\beta}}{dt} &= V_{S1} - (R_{S1} + R_{D2} + R_L)I_L(t) - V_o(t) \\ C\frac{dV_{o_\beta}}{dt} &= I_L(t) - \frac{V_o(t)}{R} \end{cases} \tag{12}$$

$$\begin{cases} L\frac{di_{L_\gamma}}{dt} &= -(R_{D1} + R_{D2} + R_L)I_L(t) - V_o(t) \\ C\frac{dV_{o_\gamma}}{dt} &= I_L(t) - \frac{V_o(t)}{R} \end{cases} \tag{13}$$

$$\begin{cases} L\frac{di_L}{dt} &= u_1(t)[V_{S1} - R_{S1}I_L(t) + R_{D1}I_L(t)] + u_2(t)[V_{S2} - R_{S2}I_L(t) + R_{D2}I_L(t)]\ldots \\ & \quad \ldots - I_L(t)[R_L + R_{D2} + R_{D1}] - V_o(t) \\ C\frac{dV_o}{dt} &= I_L(t) - \frac{V_o(t)}{R} \end{cases} \tag{14}$$

It is worth noting that Equation (14) represents a system of two dependent variables and two inputs ($u_1(t)$ and $u_2(t)$). However, the expression for output voltage on the capacitor is the same for all switching states, and it does not depend on input signal controls. Furthermore, the expression for inductor current is a nonlinear equation because its present state depends on the future state; therefore, a linearization procedure is necessary. A recursive and effective technique is linearizing the system in an interval where the nonlinear system reacts like a linear system. Such interval has an equilibrium point where the ΔV_o is null. Therefore, the expression for output voltage can be linearized as:

$$C\frac{dV_o}{dt} = 0 = I_L(t) - \frac{V_o(t)}{R} \quad \Rightarrow \quad \overline{I_L} = \frac{\overline{V_o}}{R} \tag{15}$$

Using the equilibrium point Equation (15), the states space of MISO Buck DC-DC converter expressed by (14) is redefined as:

$$\begin{cases} L\frac{di_L}{dt} &= u_1(t)\left[V_{S1} - \overline{I_L}[R_{S1} + R_{D1}]\right] + u_2(t)\left[V_{S2} - \overline{I_L}[R_{S2} + R_{D2}]\right]\ldots \\ & \quad \ldots - I_L(t)[R_L + R_{D2} + R_{D1}] - V_o(t) \\ C\frac{dV_o}{dt} &= I_L(t) - \frac{V_o(t)}{R} \end{cases} \tag{16}$$

Finally, using the superposition principle and Laplace transform on the states space of Equation (16), the transfer function for output voltage of MISO Buck DC-DC converter can be found as:

$$V_o(s) = \frac{V_{S1} - \overline{I_L}(R_{S1} - R_{D1})}{LCs^2 + \left(\frac{L}{R} + CR_p\right)s + \left(1 + \frac{R_a}{R}\right)}u_1(s) + \frac{V_{S2} - \overline{I_L}(R_{S2} - R_{D2})}{LCs^2 + \left(\frac{L}{R} + CR_p\right)s + \left(1 + \frac{R_a}{R}\right)}u_2(s) \tag{17}$$

where $R_a = R_L + R_{D1} + R_{D2}$.

On the other hand, for the MISO Flyback DC-DC converter represented in Figure 6b, the states space is defined in Equation (18) using the similar approach.

$$\begin{cases} L\frac{di_L}{dt} = u_2(t)[V_{S1} + V_{S2} - (R_{S1} + R_{S2} + R_{S3} + R_L)I_L(t)] \ldots \\ \qquad \ldots + [u_1(t) - u_2(t)][V_{S1} - (R_{S1} + R_{D2} + R_{S3} + R_L)I_L(t)] \ldots \\ \qquad \ldots + [1 - u_1(t)]\left[-\frac{(R_L + R_D)I_L(t)}{a} - aV_o(t)\right] \\ C\frac{dV_o}{dt} = \left[-\frac{V_o(t)}{R}\right]u_2(t) + \left[-\frac{V_o(t)}{R}\right][u_1(t) - u_2(t)] + \left[\frac{I_L(t)}{a} - \frac{V_o(t)}{R}\right][1 - u_1(t)] \end{cases} \tag{18}$$

Then, the dynamic model of the MISO Flyback DC-DC converter expressed in (18) can be redefined in a more simplified equation as:

$$\begin{cases} L\frac{di_L}{dt} = u_1(t)\left[V_{S1} - R_b I_L(t) - \frac{I_L(t)}{a}R_x + aV_o(t)\right] \ldots \\ \qquad \ldots + u_2(t)[V_{S2} - (R_{S2} - R_{D2})I_L(t)] - \frac{I_L(t)}{a}R_x + aV_o(t) \\ C\frac{dV_o}{dt} = \frac{I_L(t)}{a} - \frac{V_o(t)}{R} - u_1(t)\left[\frac{I_L(t)}{a}\right] \end{cases} \tag{19}$$

where $R_x = R_L + R_{D3}$ and $R_b = R_{S1} + R_{D2} + R_{S3} + R_L$.

Through the same linearization technique, the new equilibrium point for MISO Flyback DC-DC converter is obtained as:

$$\frac{\overline{I_L}}{a} = \frac{\overline{V_o}}{R(1 - \overline{u_1}).} \tag{20}$$

Therefore, using the equilibrium point of (20), the final equations for the states space this converter is expressed as:

$$\begin{cases} L\frac{di_L}{dt} = u_1(t)\left[V_{S1} - R_b\overline{I_L} - \frac{\overline{I_L}}{a}R_x + a\overline{V_o}\right] \ldots \\ \qquad \ldots + u_2(t)\left[V_{S2} - (R_{S2} - R_{D2})\overline{I_L}\right] - \frac{I_L(t)}{a}R_x + aV_o(t) \\ C\frac{dV_o}{dt} = \frac{I_L(t)}{a} - \frac{V_o(t)}{R} - u_1(t)\left[\frac{\overline{I_L}}{a}\right] \end{cases} \tag{21}$$

Similarly, using superposition and addition principle and Laplace transform on the states space represented in Equation (21), the transfer function for the output voltage of MISO Flyback DC-DC converter can be found as:

$$\begin{aligned} V_o(s) = \frac{1}{a}\left[\frac{V_{S1} - \overline{I_L}\left(R_b + \frac{R_x}{a} + R_x\right) + a\overline{V_o} - a\overline{I_L}Ls}{LCs^2 + \left(\frac{L}{R} + \frac{R_x C}{a}\right)s + \left(1 + \frac{R_x}{aR}\right)}u_1(s)\right] \\ + \frac{1}{a}\left[\frac{V_{S2} - \overline{I_L}(R_{S2} - R_{D2})}{LCs^2 + \left(\frac{L}{R} + \frac{R_x C}{a}\right)s + \left(1 + \frac{R_x}{aR}\right)}u_2(s)\right] \end{aligned} \tag{22}$$

2.3. Modelling of the Integration of Two Low-Power Renewable Energy Sources

In this section, the modeling, control and operation of two renewable energy sources (low-power photovoltaic and hydroelectric systems), and their integration as inputs to the MISO converters, are analyzed.

2.3.1. Modeling of the Photovoltaic Generation System

The photovoltaic generation system proposed as one of the power sources to evaluate the performance of the MISO DC-DC converter has the architecture shown in Figure 7. The system consists of a solar panel controlled by an incremental conductance MPPT (Maximum Point of Power Tracking) regulator. The consideration of this regulator allows the solar system to have the ability to track and obtain the maximum power for the temperature and irradiance values of the geographic location.

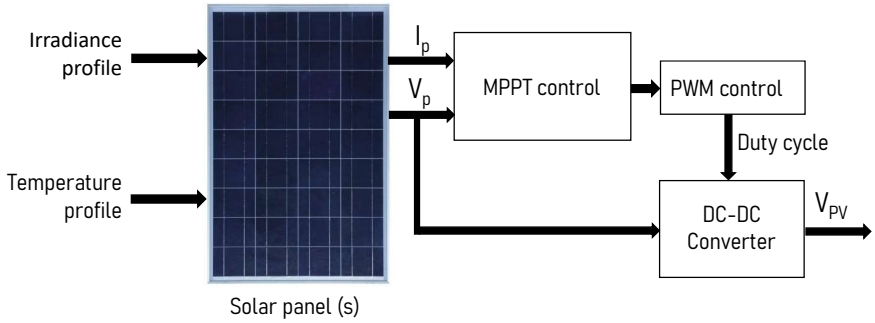


Figure 7. Architecture of the low-power photovoltaic generation system.

The starting point for the implementation of the MPPT regulator is to know the characteristic curves of the photovoltaic cell under STC conditions (standard or ideal conditions), which can be seen in Figure 8.

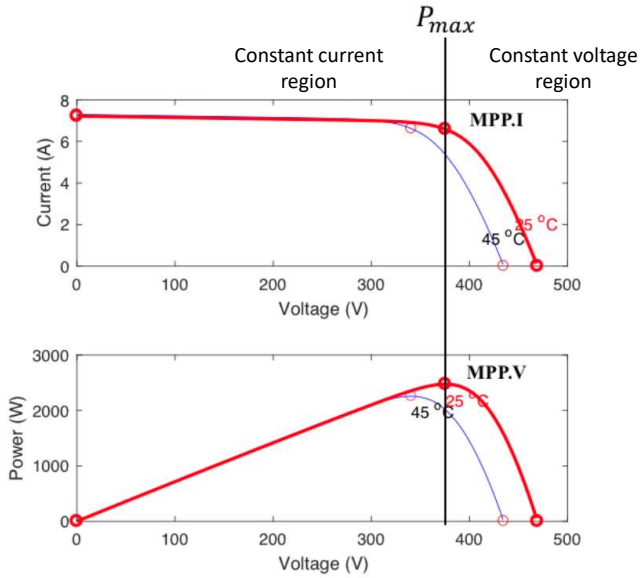


Figure 8. Current and power characteristic waveform of the solar photovoltaic panel.

According to Figure 8, the maximum power point is defined to be between the limits of the constant current and constant voltage regions. One way to reach this point is the variation of the power injected into the load, which implies a modification of voltage and current parameters through a DC-DC converter. The maximum power point, as shown in Figure 8, can be defined by (23). Therefore, when the slope in the power curve is zero, the MPP is defined by (24):

$$\frac{dP}{dV} = I + V \cdot \frac{dI}{dV} = 0 \tag{23}$$

$$\frac{dI}{dV} = -\frac{I}{V} \tag{24}$$

During the operation of the photovoltaic system, the variation of irradiance, temperature, and other factors modify the voltage, current and power curves; therefore, a continuous calculation (tracking) of the MPP (becoming MPPT) is necessary. For the case study proposed in this paper, an MPPT algorithm based on incremental conductance is proposed for decision-making regarding the increase or decrease (or steady state when reaching the MPP) of the duty cycle of the DC-DC converter attached to the photovoltaic generator. The operating principle of the incremental conductance algorithm proposed for this case is presented in Figure 9.

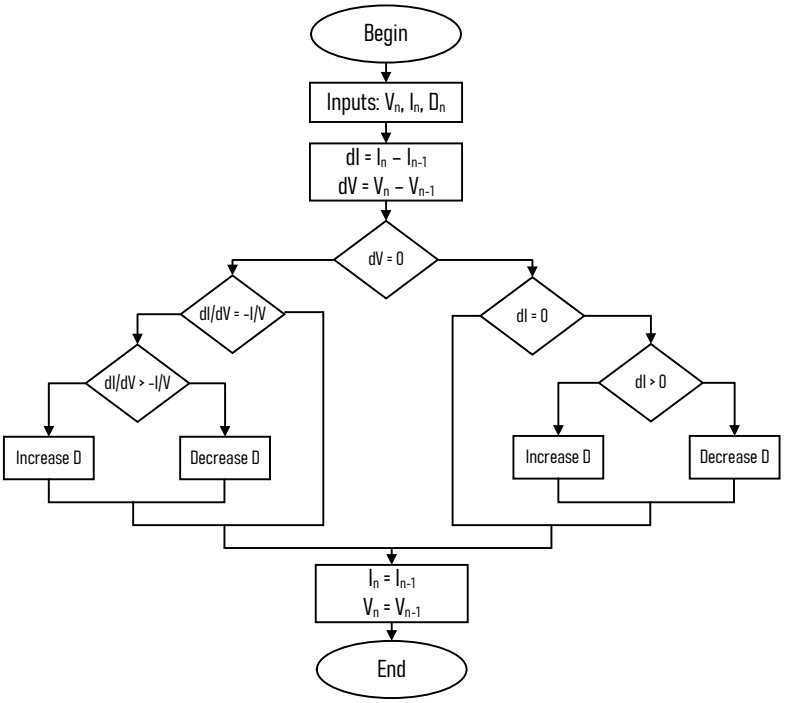


Figure 9. Incremental conductance algorithm for the MPPT regulator.

The algorithm shown in Figure 9 has been implemented in Simulink as shown in Figure 10. This representation presents a maximum power tracking algorithm with a duty cycle variation of 0.1% for each execution cycle.

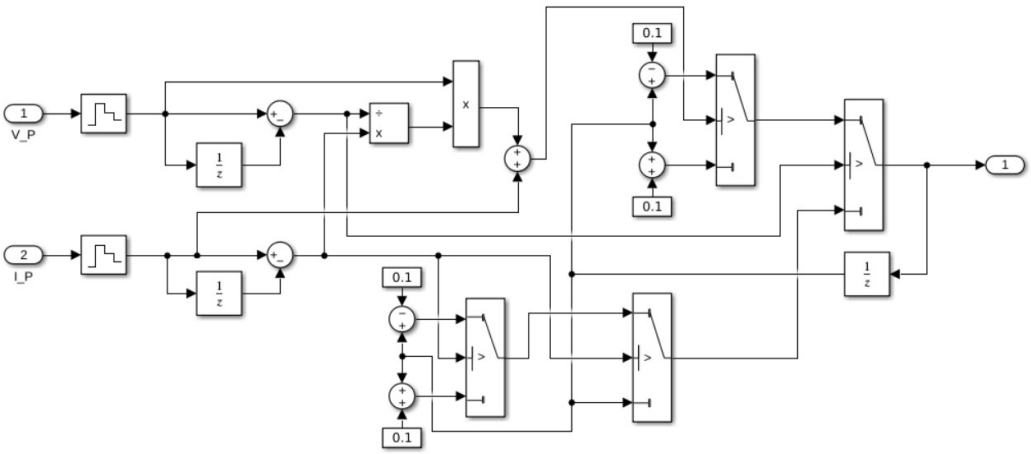


Figure 10. Simulink block diagram of the incremental conductance algorithm.

2.3.2. Modelling of the Hydroelectric Generation System

Considering the operating principles of the hydroelectric generation system, this paper presents a modeling proposal for this type of system to feed one of the input ports of the DC-DC MISO converter. The architecture of the proposed model is depicted in Figure 11.

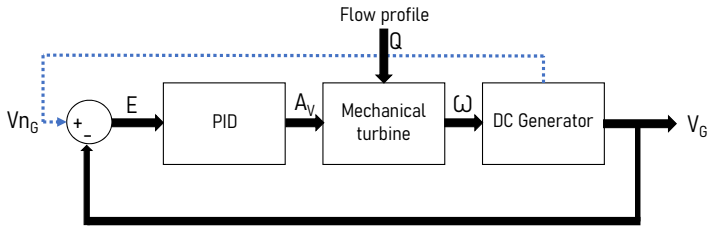


Figure 11. Architecture of the low-power DC hydroelectric generation system.

The architecture proposed in Figure 11 presents a closed-loop hydroelectric generation system based on classical controllers. This generation system operates under a flow profile, which feeds the turbine transferring its mechanical power. The turbine is mechanically coupled through its rotor to a DC generator; as a result, the DC machine is excited generating an electrical voltage at its output terminals. This system is controlled by a PID control which regulates the mechanical power delivered to the DC generator with respect to the opening of the flow inlet gate, guaranteeing a constant voltage at the output of the system. The modeling of the DC generator applied in this scenario has an equivalent circuit of the DC machine as shown in Figure 12.

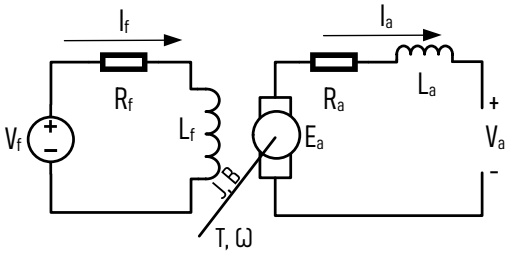


Figure 12. Equivalent circuit of the DC generator.

Based on this equivalent circuit model, the armature voltage V_a is defined as:

$$V_a = E_a + R_a I_a + L_a \frac{dI_a}{dt} \tag{25}$$

where E_a represents the armature potential, R_a is the armature resistance, I_a is the armature current, and L_a is the armature inductance.

On the one hand, applying Newton's second law, the mechanical torque T is defined by (26), with ω as the angular speed of the rotor, J is the inertial factor of the machine, and B is friction coefficient. In addition, armature potential E_a is calculated by (27). On the other hand, the mechanical torque T is also defined using (28). In this model, K_m and K_a represent the DC machine constants:

$$T = J\frac{d\omega}{dt} + B\omega \tag{26}$$

$$E_a = k_a \omega \tag{27}$$

$$T = K_m I_a \tag{28}$$

Substituting (27) in (25), the resulting expression is:

$$L_a \frac{dI_a}{dt} = V_a - R_a I_a - k_a \omega, \tag{29}$$

and replacing (28) in (26), the obtained expression is:

$$J\frac{d\omega}{dt} = k_m I_a - B\omega. \tag{30}$$

The expressions (30) and (29) represent the dynamic model of the DC generator. By applying the Laplace transform, two algebraic equations are obtained and their resolution by substitution allows for finding the transfer function of the system, which is described by (31).

$$\frac{V_a(s)}{\omega(s)} = \frac{k_m}{L_a J s^2 + (L_a B + R_a J)s + (R_a B + k_a k_m)} \tag{31}$$

To transfer mechanical power to the DC generator, it is necessary to control the flow rate hitting the turbine. Such regulation is achieved by controlling the gate opening which limits the liquid flows to the turbine. Based on this consideration, a simplified linear model of the hydraulic turbine is established as an ideal lossless turbine-penstock in which the power of the fluid flow is related to the opening of the penstock by:

$$\frac{\Delta\overline{P_m}(s)}{\Delta\overline{G}(s)} = \frac{1 - T_w s}{1 + \frac{1}{2}T_w s} \tag{32}$$

where $\overline{P_m}$ and $\overline{G}$ represent the normalized values for the turbine mechanical power and gate opening, respectively. Those parameters are based on steady-state operating point values. Moreover, T_w is the water starting time at rated load, which is a fixed value calculated by:

$$T_w = \frac{l U_r}{g H_r} \tag{33}$$

where l is the length of the water column, g is the real gate opening, U_r is the real water velocity, and H_r is the real hydraulic head at gate. More details about hydraulic turbines can be found in [27].

Therefore, the mathematical model of the hydroelectric generation system can be defined as:

$$\frac{V_a(s)}{\Delta\overline{G}(s)} = \frac{k_m}{L_a J s^2 + (L_a B + RJ)s + (R_a B + k_a k_m)} \cdot \frac{1 - T_w s}{1 + \frac{1}{2}T_w s} \tag{34}$$

Equation (34) relates the output voltage of the DC generator with respect to the opening of the gate or valve through which the fluid provides mechanical power to the electric generator. The proposed architecture corresponds to a closed-loop system as presented in Figure 11. To achieve this objective, unitary feedback is added and the PID controller is tuned, whose purpose is to pursue a reference value. For this case, the tuning was carried out using the Ziegler–Nichols method because there is a non-minimum phase system within the model as such. The proposed mathematical model has been implemented in Simulink.

2.3.3. Architecture of the Hybrid Generation System

The proposed architecture for the hybrid generation system (HGS) is presented in Figure 13. This proposal includes a closed-loop control system based on classical controllers. The purpose of the control is to set a required nominal voltage and to guarantee that such value remains constant during variations in the load profiles. For the proper operation of the process described above, the hybrid system has a security system in charge of sending control signals to the sources and the HGS isolation system, in order to safeguard the integrity of both the energy sources and the MISO DC-DC converter itself. The safety control signals of this system are processed from the duty cycles of the converter, and in case of saturation, it must shut down the system and isolate the load.

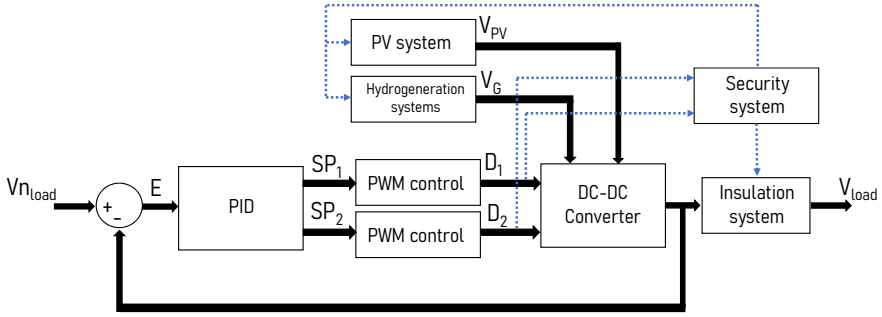


Figure 13. Proposed closed-loop control for the HGS complemented with a MISO DC-DC converter.

2.4. Sizing of the Components of the Hybrid Generation System

2.4.1. Sizing of MISO DC-DC Converters

On the one hand, the Buck-type DC-DC converter is considered as a representative of the family of non-isolated MISO DC-DC converters. The sizing includes losses in the components and the specifications for the converter's elements are detailed in Table 3. On the other hand, for the study of isolated MISO converters, the Flyback converter was considered, and its design specifications are also detailed in Table 3.

Table 3. MISO DC-DC converter parameters.

Parameters	MISO Buck		MISO Flyback	
	Values	Unit	Values	Unit
Output voltage	12–50	V	12–50	V
Input voltage	120 Max	V	120 Max	V
Frequency	25	kHz	25	kHz
Inductor	150	μH	150	μH
Capacitor	220	µF	220	µF
R (load)	10	Ω	10	Ω
R_L (coil)	120	mΩ	40	mΩ
R_D (diode)	100	mΩ	100	mΩ
R_S (switch)	47	mΩ	47	mΩ
a (N_1/N_2)			1	

2.4.2. Sizing of Photovoltaic Voltage Source

As a source of the photovoltaic generation system, a commercial solar panel module SOLARIA 225 was used, which is included in the Simscape library of Simulink. The characteristics are detailed in Table 4. The sizing of the Boost SISO converter connected to the solar panel is detailed in Table 5.

Table 4. Parameters of the solar panel.

Parameters	Values	Unit
Power	224.92	W
Cells by module	60	—
OCV	42.66	V
VMP	34.13	V
IMP	6.39	A
ISC	7.22	A
RsH	128.27	Ω
Rs	0.4994	Ω
Temperature	12–45	°C
Irradiance	1–125	kW/m^2

Table 5. Parameters of SISO boost converter.

Parameters	Values	Unit
Voltaje de Salida	25–150	V
Voltaje de entrada	80 Max	V
Inductor	10	µH
Capacitor	220	µF
Fs Max	25	KHz

2.4.3. Sizing of Hydroelectric Voltage Source

For the sizing of the hydroelectric generation system, a DC generator module is used, which is included in the Simulink library. The specifications of this module are detailed in Table 6. The values of the PID constants for the generator controller are detailed in Table 7.

Table 6. Parameters of the DC generator.

Parameters	Values	Unit
Power	5	HP
Nominal voltage (DC)	240	V
Speed	1750	rpm
Field voltage	24	V
Rf	1–50	Ω

Table 7. Parameters of the PID controller for the hydroelectric generation system.

Parameters	Values
Proportional K	0.589
Integral Ti	25.28
Derivative Td	0.001

2.4.4. Sizing of Closed-Loop Control for the Non-Isolated HGS

To obtain a closed-loop controlled HGS, the control of the MISO Buck DC-DC converter is tuned to later introduce the two generation systems into the controlled system. Under this consideration, it is analyzed through a PI controller whose tuning parameters are detailed in Table 8.

Table 8. Parameters of the PID controller for the non-isolated HGS (MISO Buck converter).

Parameters	Values
Proportional K	0.00456
Integral Ti	5.1989
Derivative Td	0

2.4.5. Sizing of Closed-Loop Control for the Isolated HGS

The closed-loop for the isolated HGS starts from the closed-loop control of the Flyback converter to later introduce the two generation systems. For the closed-loop control of the Flyback converter, the methodology proposes evaluating the system responses, resulting in a PI regulator whose parameters are detailed in Table 9.

Table 9. Parameters of the PID controller for the isolated HGS (MISO Flyback converter).

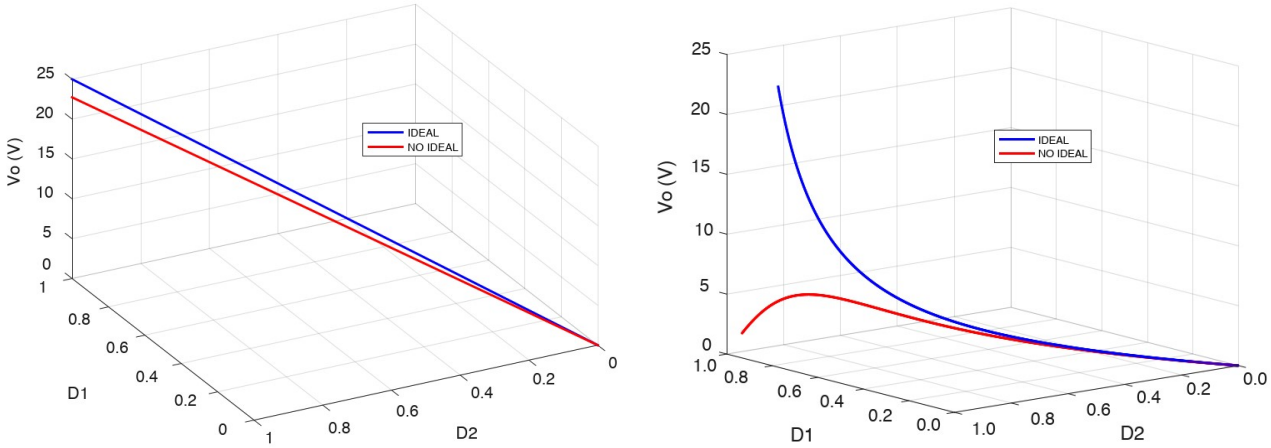
Parameters	Values
Proportional K	0.00125
Integral Ti	2.5989
Derivative Td	0

3. Results and Discussion

In this section, an efficiency analysis of the DC-DC converters that were detailed in the previous section is carried out. The objective is to describe the operating efficiency of the converters based on the main variables such as: conduction losses, commutation, number of inputs of the multiport converter and the duty cycle. Finally, the results of the case study evaluation for the integration of two renewable voltage sources through MISO DC-DC converters are presented. The results shown in this section have been analyzed and validated through simulation in both Matlab/Simulink and Psim.

3.1. Effect of Non-Ideal Components on Output Voltage

On the one hand, to show the non-ideal effect during the operation of the MISO Buck DC-DC converter, Equations (1) and (9) have been considered. On the other hand, for the MISO Flyback DC-DC converter, Equations (5) and (10) have been evaluated. The result of the comparison of both expressions is shown in Figure 14.



(**a**) Non-ideal effect on the Buck converter

(**b**) Non-ideal effect on the Flyback converter

Figure 14. Analysis of non-ideal effects on output voltage of the MISO DC-DC converters.

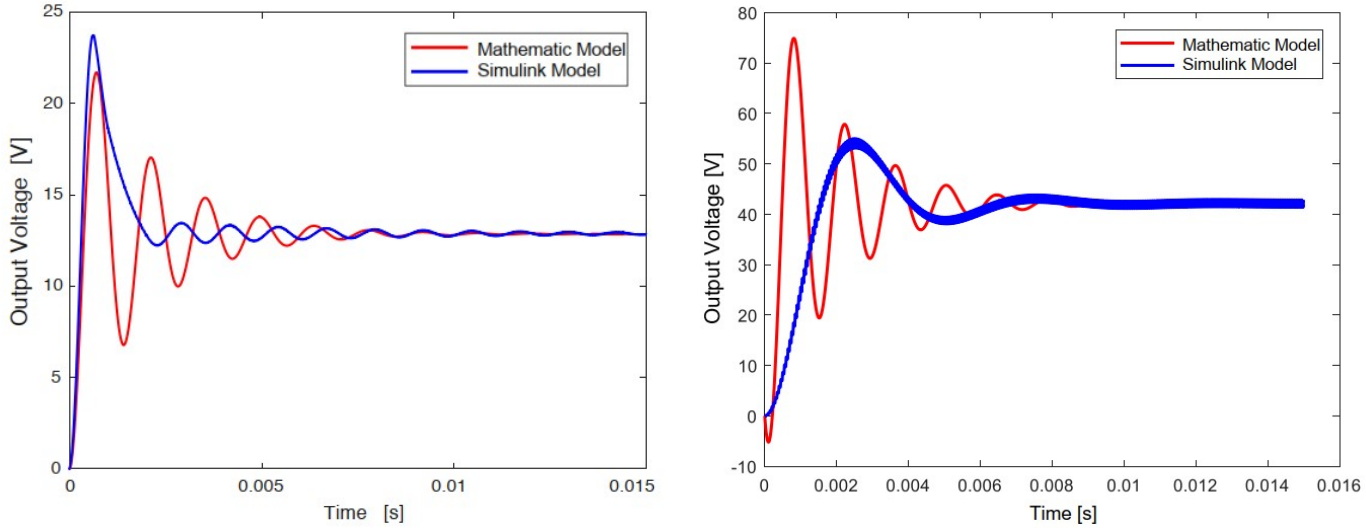
According to the results shown in Figure 14, it can be observed that the output voltage drop due to the non-ideal behavior of the switching device presents a deviation from the ideal profile; however, it is directly proportional to the supply time of each source (duty cycle). On the one hand, from this point of view, it can be established that the volume of losses increases as the duty cycle increases. On the other hand, the MISO Flyback converter exhibits a nonlinear effect while increasing the duty cycle. This way, it accumulates more losses as shown in Figure 14b, probably because it has more elements than the MISO Buck converter.

3.2. Dynamic Response of the MISO DC-DC Converters

Evaluation of the dynamic response of both DC-DC MISO converters was performed using Matlab script simulation programming for the mathematical models obtained in Section 2.2.2. Such responses were compared with transient results obtained from Simulink for circuital simulations for the MISO DC-DC converters. This comparison is very important to validate the obtained transfer functions which will be used in the next sections.

Comparison of the results from mathematical and circuit models simulations to validate the dynamical response of the MISO DC-DC converters is presented in Figure 15. By the one side, the response of transfer function of MISO DC-DC Buck converter, expressed in Equation (17), is presented in Figure 15a. By the other side, transfer function of MISO DC-DC Boost converter, according to Equation (22), is shown in Figure 15b.

In both cases, it is demonstrated that mathematical models of MISO DC-DC converters describe oscillation responses during the initial transient of the voltage conversion, but then it is attenuated until a stable or static state. This behaviour is consistent with second order systems, and it corresponds with the output voltage response obtained with circuital simulations.



(**a**) Response for MISO Buck converter (**b**) Response for MISO Flyback converter

Figure 15. Dynamic response of the output voltage of the MISO DC-DC converters.

3.3. Efficiency of Non-Ideal MISO DC-DC Converters

On the one hand, evaluation of efficiency on both MISO DC-DC converters is carried out for parallel simulation on Matlab scripting and Simulink models configured according to parameters in Table 10. Through parallel simulation, more than 500 simulations were performed for each topology with different values for duty cycles D1 and D2. On the other hand, efficiency evaluation for more than two renewable energy voltage sources is performed using PSIM software simulation.

Table 10. Efficiency of the MISO Buck converter depending on the number of ports.

Number of Ports	Duty Cycle	Efficiency %
2	$D_1 = D_2 = 0.5$	91.12
3	$D_1 = D_2 = D_3 = 0.5$	90.57
4	$D_1 = D_2 = D_3 = D_4 = 0.5$	89.28
5	$D_1 = D_2 = D_3 = D_4 = D_5 = 0.5$	87.92
6	$D_1 = D_2 = D_3 = D_4 = D_5 = D_6 = 0.5$	86.48

3.3.1. Efficiency of the MISO Buck Converter

The operating efficiency of this converter depends on several factors such as conduction losses, commutation losses, and the number of ports. In the first stage, the theoretical percentage efficiency has been identified with respect to the losses, due to the resistivity of the elements of the circuit, which is defined by Equation (35):

$$\eta\% = \frac{1}{1+\frac{R_p}{R}} = \frac{1}{1+\frac{R_L+R_{D2}(1D_2)+R_{D1}(1D_1)+R_{S1}D_1+R_{S2}D_2}{R}} \quad (35)$$

Based on Equation (35), the evaluation of efficiencies in the entire range of the spectrum of operation of duty cycles can be seen in Figure 16.

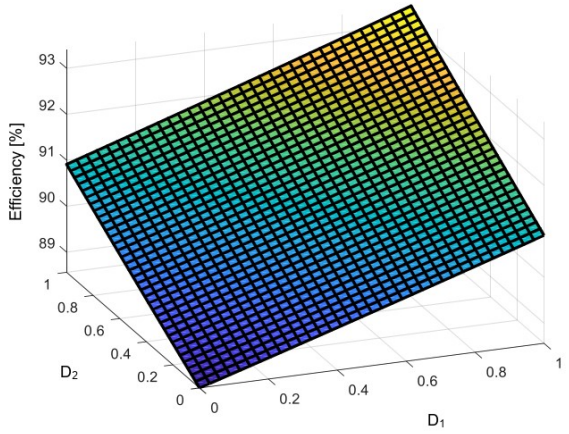
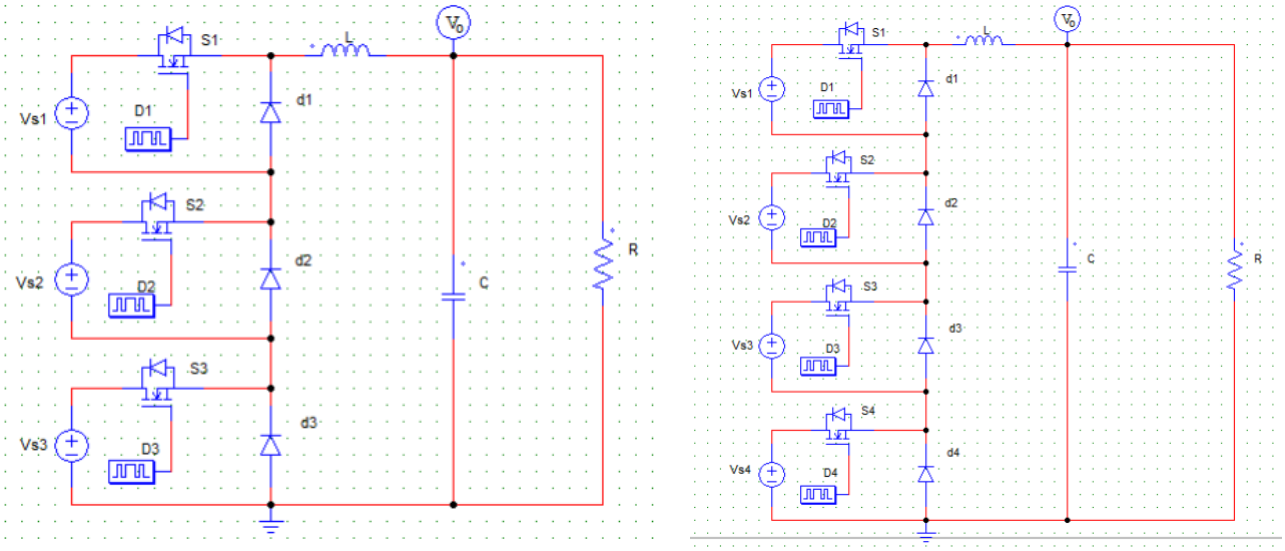


Figure 16. Efficiency surface of the non-ideal MISO Buck DC-DC converter.

It is important to note that the decrease in efficiency is linear and inversely proportional to the duty cycles D1 and D2. However, a directly proportional relationship is established between the efficiency of the system and the feeding of the load. This behavior of the system is closely related to the type of topology of the converter, taking into account that increasing the output voltage increases the current flowing to the load.

In this way, knowing that the power dissipated is directly proportional to the square of the current that circulates through the system, it is justified that the greater voltage feeding the load, the increasingly significant the effect on the performance of the converter becomes evident. Therefore, it can be seen that the performance of this converter is higher during high-duty cycles, which implies a greater increment of the output voltage.

The number of ports that the converter device has is another of the key factors that must be analyzed and considered when quantifying the efficiency. Adding more pulsating voltage source cells as inputs to the MISO converter, it increases the number of active elements and power losses affecting the performance of the converter. To evaluate this parameter, a study has been defined in which more ports are added to a buck converter sized according to the methodology provided in Section 2 but considering equal duty cycles for switches. The result of this study is detailed in Table 10, and samples of topologies considered for the multiport Buck converters are shown in Figure 17.



(**a**) Buck converter with 3 input ports

(**b**) Buck converter with 4 input ports

Figure 17. Topology of the MISO Buck converter.

According to the data shown in Table 10, the efficiency of the DC-DC MISO Buck converter decreases as inputs to the equipment are increased. To analyze the general behavior of the efficiency with respect to the number of sources, a mathematical study is formulated through simulation considering linear interpolation and extrapolation. For this analysis, the data provided in Table 10 are used to define a characteristic curve of the efficiency of the conversion system in relation to the number of ports, as shown in Figure 18 and based in Equation (36):

$$\eta\% = -1.3867np + 94.7 \tag{36}$$

Considering the results shown in Figure 18, it can be established that the reduction in efficiency presented by the converter is linearly proportional to the increase in inputs. It is important to note that the efficiency values will be different for each case study since there is a dependency on the duty cycle assigned to each input. However, the trend that marks the relationship between the efficiency of the converter and the number of inputs remains constant.

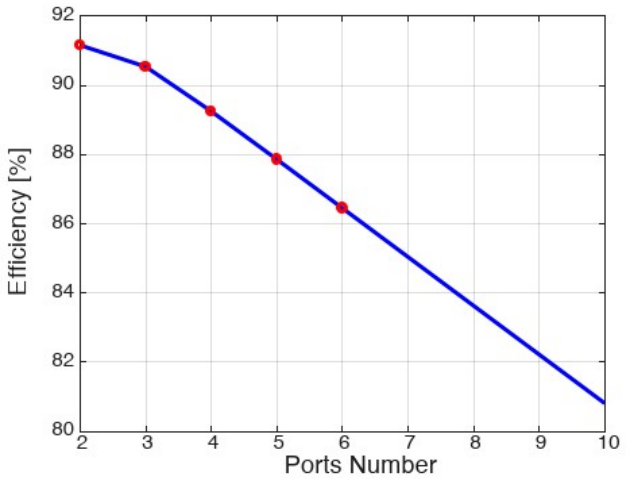


Figure 18. Converter efficiency of MISO Buck vs. Number of ports.

3.3.2. Efficiency of the MISO Flyback Converter

The efficiency study of this converter has been carried out in a similar way to the MISO Buck converter with the particularity that, for this converter, the transformation ratio $a = N_1/N_2$ between the transformer terminals has been considered as an additional parameter.

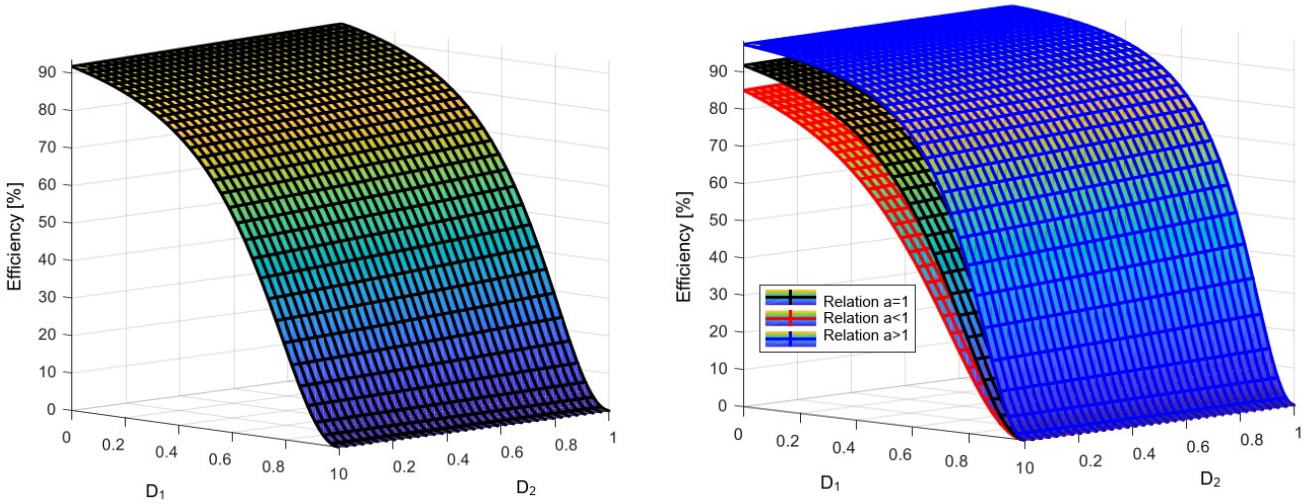
The expression that defines the theoretical percentage efficiency of this type of system is represented in Equation (37), where I_L is the average current, R_p is the conduction resistivity defined in Equation (38) and V_o in Equation (10).

$$\eta\% = \frac{\frac{V_o^2}{R}}{\frac{V_o^2}{R} + I_L^2 R_p} \cdot 100 \tag{37}$$

$$R_p = R_L D_1 + R_{D2}(D_1 - D_2) + R_{S2} D_2 + R_{S1} D_1 + R_{S3} D_1 + \frac{(1D_1)(R_L + R_{D3})}{a} \tag{38}$$

The results associated with the evaluation of Equation (37) are detailed in Figure 19, which represents the efficiency of the system with a unit transformation ratio ($a = 1$). Under this sizing criterion, the Flyback converter behaves like an isolated step-up-step-down converter. It is important to note that efficiency decreases exponentially during high-duty cycles, establishing an inversely proportional relationship between efficiency and duty cycles. Under this configuration of the Flyback converter, the operation is much more efficient when it works as a step-down converter.

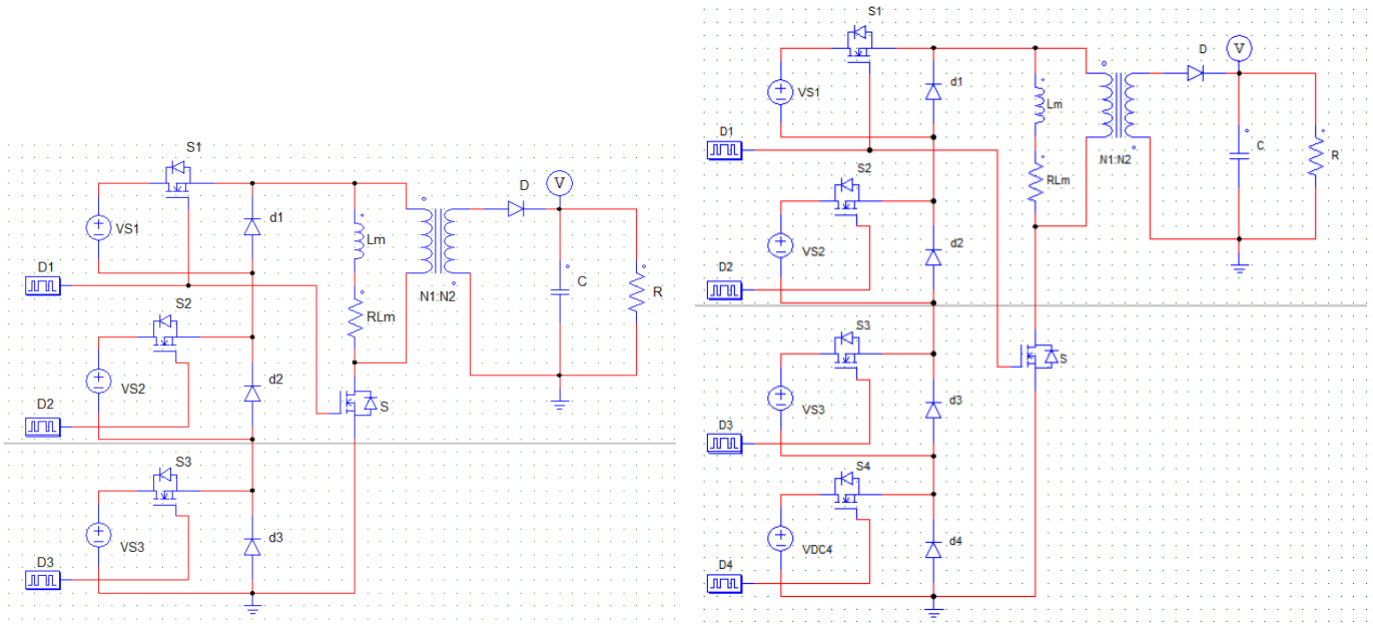
Another factor that must be taken into account for the evaluation of isolated topology converters is the transformation ratio of its transformer. This relationship has a direct impact on the efficiency of the system as shown in Figure 19, in which it is evident that, by reducing the transformation ratio, the efficiency of the system drastically decreases. When the transformation ratio exceeds unity, the efficiency of the system improves significantly, making the Flyback converter operate at high efficiency for high-duty cycle values.



(**a**) Efficiency related with the unit transformation (**b**) Efficiency related with different transformer relation

Figure 19. Efficiency surfaces of the non-ideal MISO Flyback converter.

The efficiency of DC-DC MISO converters also depends on the number of inputs that the converter has. To demonstrate the effect that the number of ports has on the efficiency during operation, an evaluation of the Flyback converter has been proposed, which has been dimensioned according to section A considering a unitary transformation ratio. The details of the results of this study are shown in Table 11 for the different number of input ports, while samples of multiport topologies considered are detailed in Figure 20.



(**a**) Flyback converter with 3 input ports (**b**) Flyback converter with 4 input ports

Figure 20. Topology of the MISO Flyback converter.

Table 11. Efficiency of the MISO Flyback converter depending on the number of ports.

Number of Ports	Duty Cycle	Eficiency %
2	$D_1 = D_2 = 0.5$	88.42
3	$D_1 = D_2 = D_3 = 0.5$	87.37
4	$D_1 = D_2 = D_3 = D_4 = 0.5$	86.53
5	$D_1 = D_2 = D_3 = D_4 = D_5 = 0.5$	86.31

In Table 11, it can be seen that the number of ports has an effect on the efficiency of the converter, which is reduced as the input sources increase. To study the behavior of the efficiency reduction, mathematical analysis has been defined considering the linear interpolations that allow for obtaining the characteristic curve of the efficiency of the converter vs. the number of ports as described in Equation (39) from the data shown in Table 11. The result of this analysis can be seen in Figure 21.

$$\eta\%_{np} - 0.5757np + 88.9814 \tag{39}$$

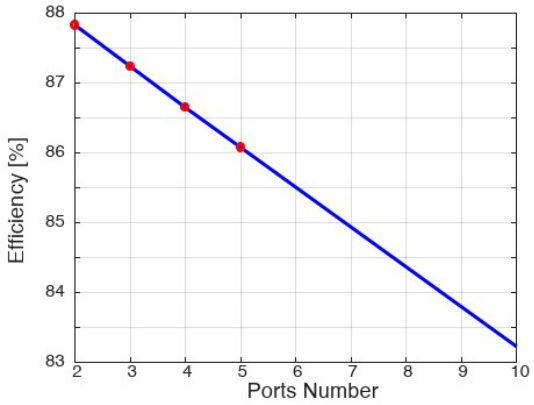


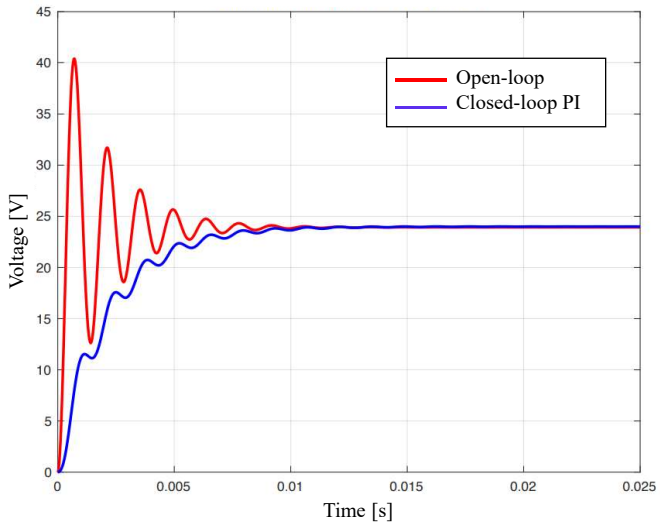
Figure 21. Converter efficiency of MISO Flyback vs. Number of ports.

As a result of this study, it can be seen that the number of additional inputs to the converter does not have a significant effect on the efficiency of the converter. This effect is due to the fact that the duty cycles are balanced as well as their magnitude in each of the sources connected to the input of the converter. This study shows that the number of ports decreases the efficiency of the system in a linear way. The magnitude of this linearity will depend on the particular case considering the duty cycle and the magnitude of the source that is connected to the converter.

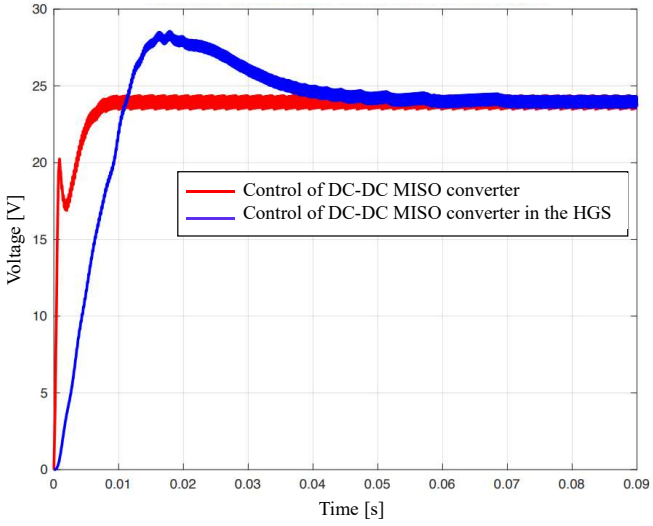
3.4. Response of Closed-Loop Control for HGS

3.4.1. Closed-Loop Control for the Non-Isolated HGS

The response of the system in a closed-loop for the MISO buck converter according to the parameters established in Table 8 is depicted in Figure 22a. Note that, with a PI controller, the reference tracking is achieved without getting overshot and with an acceptable settling time. From the implementation of HGS in Simulink, the response of the closed-loop system based is evaluated, and its result is shown in Figure 22b. Note that the responses differ during the transient; this is because when the controller was tuned the transient of the sources was not initially considered. However, once the hybrid energy generation system is operating, this disturbance is considered since each generation system presents transients.



(**a**) MISO Buck converter response.

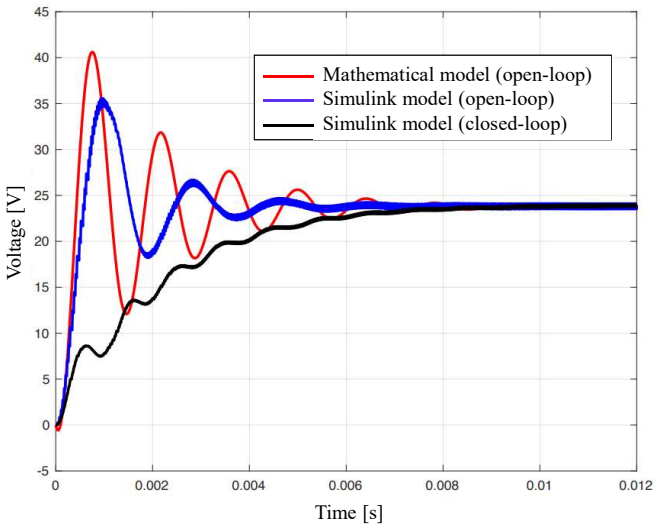


(**b**) Non-isolated HGS response.

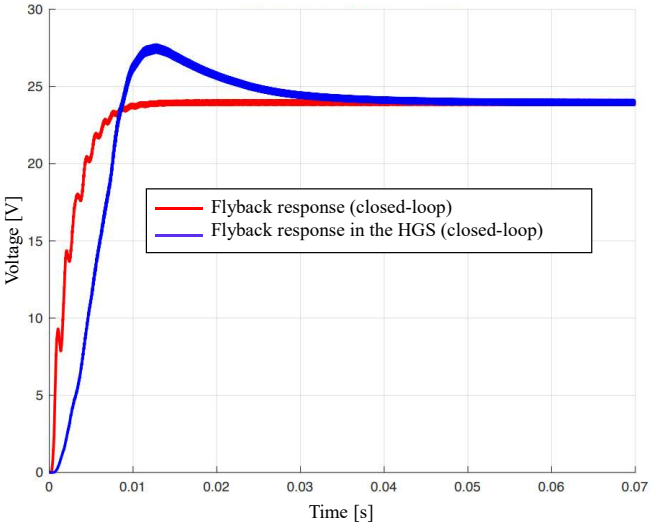
Figure 22. Response evaluation of MISO Buck converter and non-isolated HGS.

3.4.2. Closed-Loop Control for the Isolated HGS

From the model implemented in Simulink and mathematical modeling, the response of the closed-loop system compared to the opened-loop system is evaluated and depicted in Figure 23a. In addition, in Figure 23b, a brief difference is observed between the closed-loop system response of the Flyback converter and the closed-loop HGS response. This is associated with different factors such as: input voltage variability, transient state of generation systems, reference changes, etc. However, it can be seen that the HGS presents a sensitive and robust response to input disturbances.



(**a**) MISO Flyback converter response

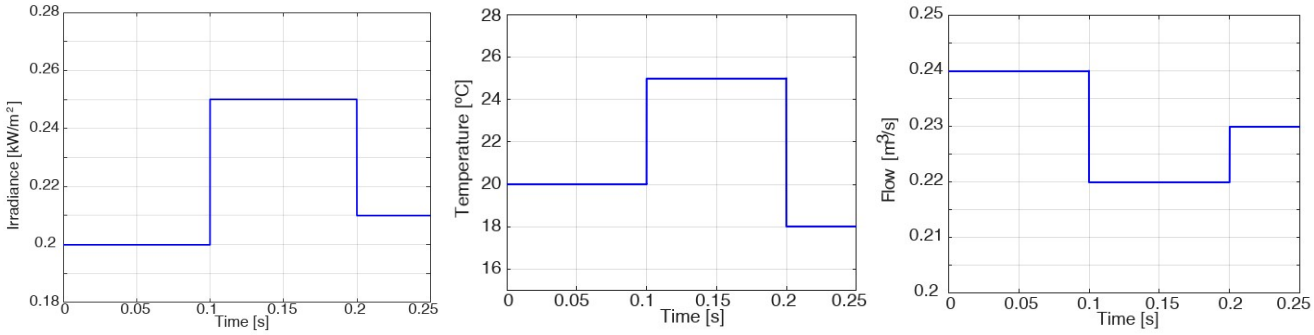


(**b**) Non-isolated HGS response

Figure 23. Response evaluation of MISO Flyback converter and non-isolated HGS.

3.5. Performance of the MISO DC-DC Converter on an HGS

In this subsection, the performance of DC-DC conversion systems is evaluated under a hybrid energy generation scenario. For the evaluation of the proposed models, the irradiance, temperature and flow input profiles are established as those shown in Figure 24a–c, respectively.



(**a**) Irradiance profile (**b**) Temperature profile (**c**) Fluid flow profile

Figure 24. Input profiles for the HGS system validation.

This scenario evaluates the HGS considering the input profiles shown in Figure 24. Under these established conditions, the photovoltaic and hydroelectric voltage generation system's behavior is shown in Figure 25. It is worth noting that generated photovoltaic voltage is higher than a hydroelectric generation, but also is highly sensitive to the changes in irradiance and temperature profiles, which is related to the operation of the MPPT algorithm. The hydroelectric voltage remains stable in the generation, even the changes in the flow, because the close-loop control for the turbine regulates the opening of the gate to compensate.

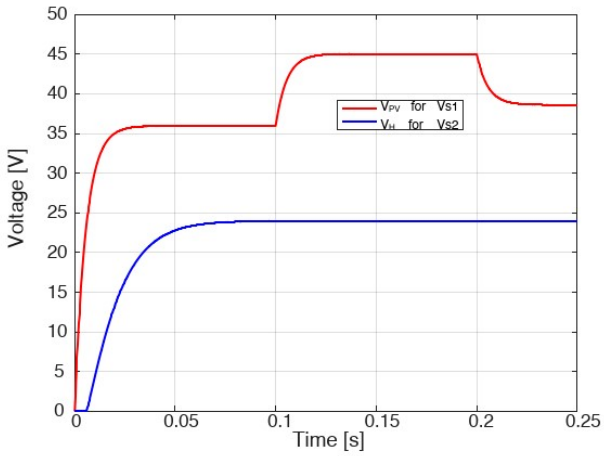
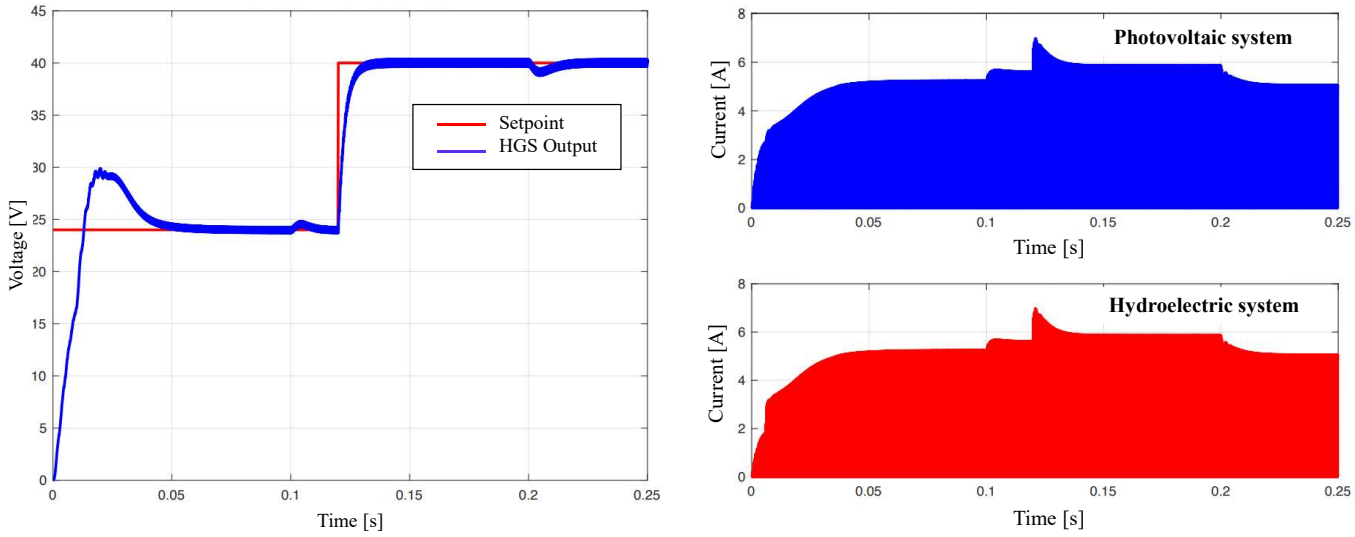


Figure 25. Photovoltaic (red-line) and hydroelectric (blue-line) input voltage levels to the HGS.

3.5.1. HGS Based on Non-Isolated MISO DC-DC Converter

Based on the values of V_{PV} for V_{S1} and V_H for V_{S2} power sources and considering a sudden change in the nominal load requirement from 24 VDC to 40 VDC, the output voltage of the HGS is shown in Figure 26a when a MISO Buck DC-DC converter is used.

Observe that, before the sudden reference change, at instant t = 0.12 s, the system responds in an over-damped way with a short settling time and without over-elongation to this setpoint. This response is due to the fact that, for this instant of time, the two generation systems are already in a permanent regime, making it easier for the controller to follow the desired reference under the response model for which it was designed. Under a reference change, the currents supplied to the system are as shown in Figure 26b.



(**a**) (**b**)

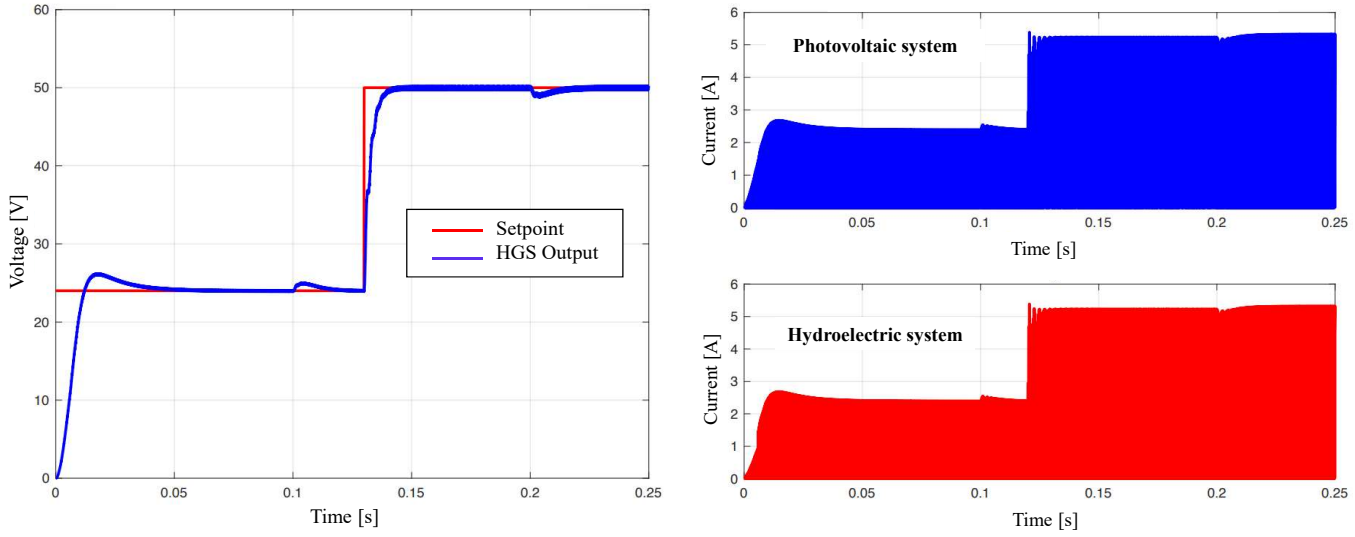
Figure 26. HGS output (non-isolated) under setpoint change: (**a**) Voltage and (**b**) Current.

3.5.2. HGS Based on an Isolated DC-DC Converter

This scenario also evaluates the HGS considering the input voltage profiles shown in Figure 25 and the integration of voltage sources through the MISO Flyback DC-DC converter.

In Figure 27a, the response of the system to the reference change can be observed with a setting without oscillations in the transient and with a shorter settling time compared to when the system reached the initial reference.

The current supplied by the generation sources in this scenario is shown in Figure 27b. This figure shows that, before a sudden reference change, the control system demands a higher current to cover the supply of the new nominal voltage. In addition, note that there are no current peaks during the reference change transient because the voltage rise corresponds to the rate of current rise.

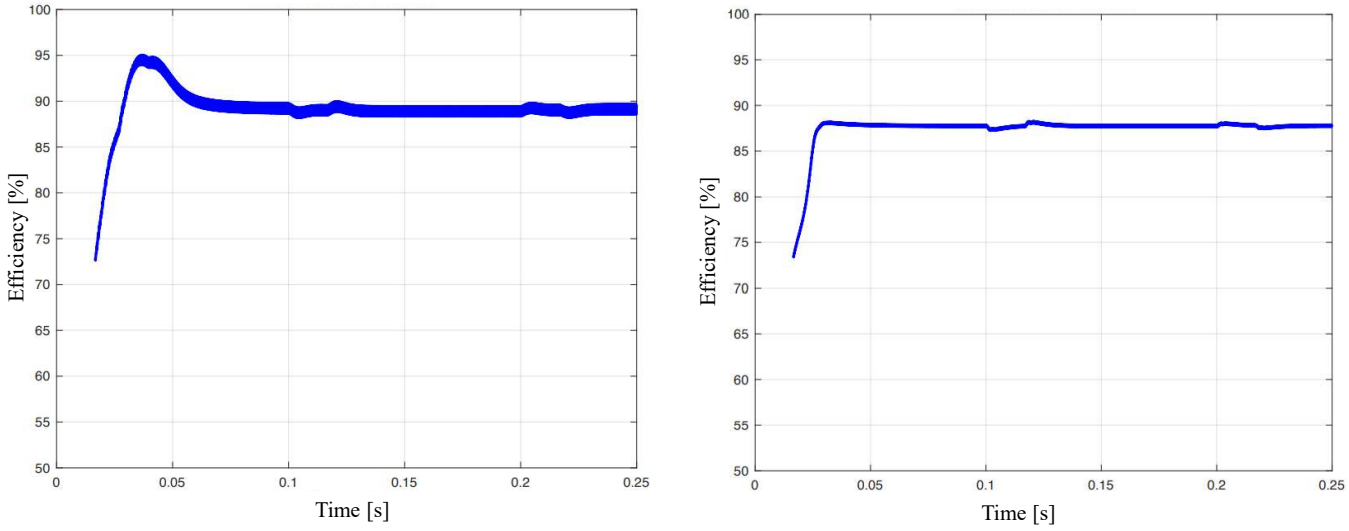


(**a**) (**b**)

Figure 27. HGS output (isolated) under setpoint change: (**a**) Voltage and (**b**) Current.

3.6. Efficiency of the HGS with Closed-Loop Control

This section shows the response of the HGS in terms of efficiency applying a closed-loop control. For the system based on a non-isolated converter, the efficiency curve is shown in Figure 28a.



(**a**) (**b**)

Figure 28. Efficiency of the DC-DC converter in the HGS: (**a**) non-isolated architecture and (**b**) isolated architecture.

Considering the results shown in Figure 28a, it can be established that the efficiency for the proposed case study (applying a closed-loop control) reaches an average value of 88% in the power transfer supplied by each of the generation sources. On the other hand, for the system based on an isolated converter, the efficiency curve is shown in Figure 28b. In this case, the DC-DC converter achieves an efficiency greater than 85% in the transfer of power from the sources to the load, which makes it a system with acceptable efficiency for the application of the closed-loop control.

3.7. A Comparison Analysis of Multiple Input DC-DC Converters in the Literature

In this section, a comparative analysis of studies related to the presented work on multiple input converters is carried out. The purpose of this comparison is to clarify and highlight the importance of the study developed. Table 12 shows a summary of some manuscripts focused on the study of multi input DC-DC converters.

Table 12. Related works summary table.

Reference	DC-DC Topologies Studied	Description	Main Focuses
[10]	- Buck–Boost - Sepic - Cuk - Z-source - Zeta	- Analysis of non-isolated DC-DC converters - Modelling of non-isolated converters - Topology efficiency study considering duty cycle and load - Comparison of advanced control techniques	- Non-isolated DC-DC converters and advanced control techniques

Table 12. *Cont.*

Reference	DC-DC Topologies Studied	Description	Main Focuses
[28]	- General consideration of non-isolated and isolated converters	- DC-DC converter comparisons considering components - ZVS study for increasing the efficiency - Control strategy study - Efficiency study based on control technique analysis	- Multi-input DC-DC converters focused on control strategy and ZVS for increasing the converter efficiency
[19]	- Multiport buck-boost converter with isolated and non-isolated port - Bidirectional multiport converter - Bidirectional LLC power converter	- Model and characteristics analysis of DC-DC converters - DC-DC converter application analysis - Analysis of Characteristics of multi-input DC-DC converters - Challenges and future trends	- Review of the DC-DC converter topologies for Electric Vehicles and Renewable energy
[9]	- Topologies of non-isolated and isolated DC-DC converters	- Topologies comparison, characteristics and operation modes - Application study in a microgrid converters - Future trends for DC-DC converters in microgrid application	- A general review of non-isolated and isolated DC-DC converters
This work	- Buck - Flyback	- Multi-input isolated and non-isolated converters modeling and design methodology - Efficiency analysis considering non-idealities - Analysis with real models of the energy generation systems - Control design and performance evaluation under load variation	- Design methodology and a comprehensive efficiency study for increasing the performance of simple multi-input DC-DC converters considering, real sources models, non-idealities, load variation and simple control

Some similar works were found in the literature and are summarized in Table 12. According to the information presented, there is no study that has considered all the factors presented in this work and some are focused only on control strategies. This demonstrates the importance of the analysis developed in this manuscript and the importance of the results obtained.

4. Conclusions

In this paper, the efficiency of both isolated and non-isolated DC-DC MISO converters was analyzed. The proposed analysis methodology is based on the design strategy of multiport type converters by combining a pulsing voltage source cell (PVSC) which can be integrated into a basic topology converter. Different topologies of converters were analyzed: Buck and Flyback, which represent non-isolated and isolated topologies.

The consideration of the analyzed design strategy is based on the development of DC-DC MISO converters with: a reduced number of components, simple topologies, high-frequency transformers with a single primary winding (isolated architecture), a single coil,

the ability to control the flow of energy from the source individually or simultaneously (several inputs) and flexibility in sizing the capacity of the source.

In this way, in the present work, multiple input DC-DC converters have been proposed with a simple and compact structure and with fault tolerance capacity that improves the efficiency and reliability of the converter. In addition, the information provided in this study allows the design of converters that better manage energy and operation when multi-input topologies are considered for low-power sources integration.

The efficiency study of the conversion systems considered factors such as: the number of converter inputs, duty cycle associated with the primary sources, transformation ratio (isolated architecture) and mode of operation (Flyback and Buck). The results obtained show that the non-isolated architecture is more efficient than the isolated architecture but with a lower degree of protection in the power flows from the sources to the load.

Author Contributions: Conceptualization, J.S.-G. and J.H.-A.; methodology, J.H.-A.; software, J.S.-G.; validation, V.H.-P. and M.P.-C.; formal analysis, V.H.-P. and J.H.-A.; data curation, M.D.-P. and A.P.-C.; original draft preparation, V.H.-P. and J.H.-A. All authors have read and agreed to the published version of the manuscript.

Funding: This research received no external funding.

Data Availability Statement: No new data were created or analyzed in this study. Data sharing is not applicable to this article.

Conflicts of Interest: The authors declare no conflict of interest.

References

1. Akizu-Gardoki, O.; Bueno, G.; Wiedmann, T.; Lopez-Guede, J.M.; Arto, I.; Hernandez, P.; Moran, D. Decoupling between human development and energy consumption within footprint accounts. *J. Clean. Prod.* **2018**, *202*, 1145–1157. [CrossRef]
2. Acar, C.; Dincer, I. Environmental impact assessment of renewables and conventional fuels for different end use purposes. *Int. J. Glob. Warm.* **2017**, *13*, 260–277. [CrossRef]
3. Umayal, S.P.; Selvakumar, P.; Ramkumar, V. Multiple input Fuzzy controlled DC-DC Converter for harvesting renewable energy. In Proceedings of the 2021 7th International Conference on Electrical Energy Systems (ICEES), Virtual, 11–13 February 2021; Volume 6, pp. 329–333. [CrossRef]
4. Hossain, M.; Rahim, N. Recent progress and development on power DC-DC converter topology, control, design and applications: A review. *Renew. Sustain. Energy Rev.* **2018**, *81*, 205–230. [CrossRef]
5. Qais, M.H.; Hasanien, H.M.; Alghuwainem, S. A novel LMSRE-based adaptive PI control scheme for grid-integrated PMSG-based variable-speed wind turbine. *Int. J. Electr. Power Energy Syst.* **2021**, *125*, 106505. [CrossRef]
6. Butt, O.M.; Zulqarnain, M.; Butt, T.M. Recent advancement in smart grid technology: Future prospects in the electrical power network. *Ain Shams Eng. J.* **2021**, *12*, 687–695. [CrossRef]
7. Rehman, Z.; Al-Bahadly, I.; Mukhopadhyay, S. Multiinput DC–DC converters in renewable energy applications—An overview. *Renew. Sustain. Energy Rev.* **2015**, *41*, 521–539. [CrossRef]
8. Kolli, A.; Gaillard, A.; De Bernardinis, A.; Bethoux, O.; Hissel, D.; Khatir, Z. A review on DC/DC converter architectures for power fuel cell applications. *Energy Convers. Manag.* **2015**, *105*, 716–730. [CrossRef]
9. Alhurayyis, I.; Elkhateb, A.; Morrow, J. Isolated and nonisolated DC-to-DC converters for medium-voltage DC networks: A review. *IEEE J. Emerg. Sel. Top. Power Electron.* **2020**, *9*, 7486–7500. [CrossRef]
10. Mumtaz, F.; Yahaya, N.Z.; Meraj, S.T.; Singh, B.; Kannan, R.; Ibrahim, O. Review on non-isolated DC-DC converters and their control techniques for renewable energy applications. *Ain Shams Eng. J.* **2021**, *12*, 3747–3763. [CrossRef]
11. Arunkumari, T.; Indragandhi, V. An overview of high voltage conversion ratio DC-DC converter configurations used in DC micro-grid architectures. *Renew. Sustain. Energy Rev.* **2017**, *77*, 670–687. [CrossRef]
12. Qi, Q.; Ghaderi, D.; Guerrero, J.M. Sliding mode controller-based switched-capacitor-based high DC gain and low voltage stress DC-DC boost converter for photovoltaic applications. *Int. J. Electr. Power Energy Syst.* **2021**, *125*, 106496. [CrossRef]
13. Choudhury, T.R.; Nayak, B.; Santra, S.B. Investigation of voltage stress on a single switch boost-fly-back integrated high gain converter with light load condition. *Ain Shams Eng. J.* **2019**, *10*, 217–226. [CrossRef]
14. Wang, Y.; Tian, J.; Sun, Z.; Wang, L.; Xu, R.; Li, M.; Chen, Z. A comprehensive review of battery modeling and state estimation approaches for advanced battery management systems. *Renew. Sustain. Energy Rev.* **2020**, *131*, 110015. [CrossRef]
15. Schellekens, J.M.; Huisman, H.; Duarte, J.L.; Hendrix, M.A.; Lomonova, E.A. An analysis of the highly linear transfer characteristics of dual-buck converters. *IEEE Trans. Ind. Electron.* **2017**, *65*, 4681–4690. [CrossRef]
16. Tekin, H.; Bulut, K.; Ertekin, D. A novel switched-capacitor and fuzzy logic-based quadratic boost converter with mitigated voltage stress, applicable for DC micro-grid. *Electr. Eng.* **2022**, *104*, 4391–4413. [CrossRef]

17. Veerachary, M.; Trivedi, A. Linear Matrix Inequality-Based Multivariable Controller Design for Boost Cascaded Charge-Pump-Based Double-Input DC–DC Converter. *IEEE Trans. Ind. Appl.* **2022**, *58*, 7515–7528. [CrossRef]
18. ELhagry, M.M.; Elkady, Z.; Abdel-Rahim, N.; Bendary, F. New topology of multiple-input single-output PV system for DC load applications. *J. Electr. Syst. Inf. Technol.* **2016**, *3*, 471–484. [CrossRef]
19. Affam, A.; Buswig, Y.M.; Othman, A.K.B.H.; Julai, N.B.; Qays, O. A review of multiple input DC-DC converter topologies linked with hybrid electric vehicles and renewable energy systems. *Renew. Sustain. Energy Rev.* **2021**, *135*, 110186. [CrossRef]
20. Raj, A.; Praveen, R. Highly efficient DC-DC boost converter implemented with improved MPPT algorithm for utility level photovoltaic applications. *Ain Shams Eng. J.* **2022**, *13*, 101617. [CrossRef]
21. Alsolami, M. A multi-input, multi-stage step-up DC-DC converter for PV applications. *Alex. Eng. J.* **2021**, *60*, 2315–2324. [CrossRef]
22. Khosrogorji, S.; Ahmadian, M.; Torkaman, H.; Soori, S. Multi-input DC/DC converters in connection with distributed generation units—A review. *Renew. Sustain. Energy Rev.* **2016**, *66*, 360–379. [CrossRef]
23. Cheng, T.; Lu, D.D.; Gong, A.; Verstraete, D. Analysis of a three-port DC-DC converter for PV-battery system using DISO boost and SISO buck converters. In Proceedings of the 2015 Australasian Universities Power Engineering Conference (AUPEC), Wollongong, NSW, Australia, 27–30 September 2015; pp. 1–6.
24. Kumar, S.S.; Nirmal, M.C.M.; Jayaprakash, P. Power Management of a Grid Interactive PV - Fuel Cell Hybrid System with Power Dispatch to the Grid Using Modified LMS Control. In Proceedings of the 2020 IEEE International Conference on Power Electronics, Drives and Energy Systems (PEDES), Jaipur, India, 16–19 December 2020; pp. 1–6. [CrossRef]
25. Yalamanchili, K.P.; Ferdowsi, M.; Corzine, K. New Double Input DC-DC Converters for Automotive Applications. In Proceedings of the 2006 IEEE Vehicle Power and Propulsion Conference, Windsor, UK, 6–8 September 2006; pp. 1–6. [CrossRef]
26. Wang, Q.; Zhang, J.; Ruan, X.; Jin, K. A Double-input flyback DC/DC converter with single primary winding. In Proceedings of the 2010 IEEE Energy Conversion Congress and Exposition, ECCE 2010—Proceedings, Atlanta, GA, USA, 12–16 September 2010; pp. 1938–1944. [CrossRef]
27. Ordys, A.W.; Pike, A.; Johnson, M.A.; Katebi, R.M.; Grimble, M.J. *Modelling and Simulation of Power Generation Plants*; Springer Science & Business Media: New York, NY, USA, 2012.
28. Madhana, R.; Mani, G. Power enhancement methods of renewable energy resources using multiport DC-DC converter: A technical review. *Sustain. Comput. Inform. Syst.* **2022**, *35*, 100689. [CrossRef]

Disclaimer/Publisher's Note: The statements, opinions and data contained in all publications are solely those of the individual author(s) and contributor(s) and not of MDPI and/or the editor(s). MDPI and/or the editor(s) disclaim responsibility for any injury to people or property resulting from any ideas, methods, instructions or products referred to in the content.